

Review Article

Layer-specific anatomical, physiological and functional MRI of the retina

Timothy Q. Duong,^{1,4*} Mabelle T. Pardue,^{2,4} Peter M. Thulé,^{3,4} Darin E. Olson,^{3,4} Haiying Cheng,¹ Govind Nair,¹ Yingxia Li,¹ Moon Kim,⁴ Xiaodong Zhang¹ and Qiang Shen¹

¹Departments of Neurology and Radiology, Yerkes Imaging Center

²Department of Ophthalmology, Emory University, Atlanta, GA, USA

³Department of Medicine, Division of Endocrinology, Metabolism & Lipids, Emory University, Atlanta, Emory University, Atlanta, GA, USA

⁴Atlanta Veterans Affairs Medical Center, Decatur, GA, USA

Received 20 May 2008; Revised 16 June 2008; Accepted 19 June 2008

ABSTRACT: Most retinal imaging has been performed using optical techniques. This paper reviews alternative retinal imaging methods based on MRI performed with spatial resolution sufficient to resolve multiple well-defined retinal layers. The development of these MRI technologies to study retinal anatomy, physiology (blood flow, blood volume, and oxygenation) and function, and their applications to the study of normal retinas, retinal degeneration and diabetic retinopathy in animal models are discussed. Although the spatiotemporal resolution of MRI is poorer than that of optical imaging techniques, it is unhampered by media opacity and can thus image all retinal and pararetinal structures, and has the potential to provide multiple unique clinically relevant data in a single setting and could thus complement existing retinal imaging techniques. In turn, the highly structured retina with well-defined layers is an excellent model for advancing emerging high-resolution anatomical, physiological and functional MRI technologies. Copyright © 2008 John Wiley & Sons, Ltd.

KEYWORDS: choroid; retinal blood flow; BOLD; functional MRI; diffusion-weighted MRI; high resolution imaging; retinal diseases; manganese-enhanced MRI (MEMRI)

RETINAL ANATOMY AND PHYSIOLOGY

Anatomical layers

The retina consists of multiple well-defined layers (1–3). Starting from the vitreous boundary, they include the ganglion cell layer (GCL), inner plexiform layer (IPL), inner nuclear layer (INL), outer plexiform layer (OPL), outer nuclear layer (ONL), and photoreceptor inner and

outer segments (IS + OS) (Fig. 1, rat retina). The plexiform layers are synaptic links between adjacent nuclear cell layers.

Vascular layers

The retina is nourished by two separate blood supplies: the retinal and choroidal circulations (1,4,5). Retinal vessels exist in the GCL, INL, IPL and OPL. Choroidal vessels do not exist in the neural retina, but rather are located posterior to the photoreceptor layer, sandwiched between the retinal pigment epithelium and sclera. Thus, the ONL and IS + OS are avascular, relying on diffusion, predominantly from the choroidal circulation, for oxygen delivery (1,4,5). In fact, oxygen tension in the middle of the retina is close to zero under normal physiological conditions (6–8) probably because of the high oxidative demands of the photoreceptors and their dependence on diffusive oxygen transport (1,4,5). The total retinal thickness across multiple mammalian species, excluding the choroid, has been reported to be ~217 µm (2,3) and the choroidal thickness, which is less well documented, has been reported to be 25–45 µm (9) from histological examination in rats.

*Correspondence to: T. Q. Duong, Emory University, Yerkes Imaging Center, Division of Neuroscience, Yerkes Research Center, 954 Gatewood Rd NE, Atlanta, Georgia, United States 30329.
E-mail: tduong@emory.edu

Contract/grant sponsor: NIH/NEI; contract/grant number: R01 EY014211.

Contract/grant sponsor: Whitaker Foundation; contract/grant number: RG-02-0005.

Contract/grant sponsor: Department of Veterans Affairs, Emory University Research Committee NIH/NEI Ophthalmology Core; contract/grant numbers: P30 EY006360, NIH/NCRR P51 RR000165.

Contract/grant sponsor: Woodruff Health Science Center.

Abbreviations used: ADC, apparent diffusion coefficient; ASL, arterial spin labeling; BOLD, blood oxygenation level dependent; fMRI, functional MRI; GCL, ganglion cell layer; GdDTPA, gadolinium diethylenetriaminepenta-acetic acid; INL, inner nuclear layer; IPL, inner plexiform layer; IS + OS, photoreceptor inner and outer segments; MEMRI, manganese-enhanced MRI; ONL, outer nuclear layer; OPL, outer plexiform layer; RCS, Royal College of Surgeons; STZ, streptozotocin.

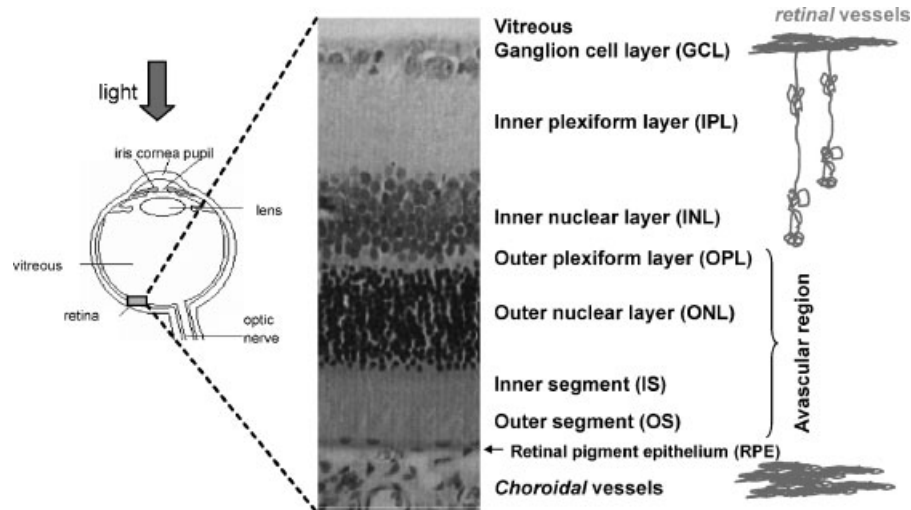


Figure 1. Cartoon of the eye and histology of rodent retina. The retina consists of multiple well-defined layers (1–3). Starting from the vitreous boundary, they include the GCL, IPL, INL, OPL, ONL, and IS + OS. The retina is nourished by two separate blood supplies: the retinal and choroidal circulations. The retinal vessels exist within the GCL, INL, IPL and OPL. The choroidal vessels are located posterior to the photoreceptor layer. The ONL and IS + OS are avascular.

Although both vasculatures are required for proper retinal function, blood flow is regulated differently in the retinal and choroidal vessels. Basal choroidal blood flow is many times higher than retinal blood flow and responds uniquely to many regulating factors (1,4,5,10,11). In contrast, retinal blood flow is similar to cerebral blood flow, and responds similarly to regulating factors as in the brain. For example, hyperoxia markedly decreases retinal blood flow (vasoconstriction), and hypercapnia markedly increases retinal blood flow (vasodilation), whereas hyperoxia and hypercapnia have smaller effects on choroidal blood flow. The high choroidal blood flow may be in excess of local metabolic requirements, and may be necessary to maintain a large oxygenation gradient (12) and to dissipate heat produced by light (13,14).

Existing optical techniques

With a few exceptions, the retina has been historically studied *in vivo* using optically based imaging techniques to study anatomy [fundus imaging, scanning laser ophthalmoscopy and optical coherence tomography (15)] or image blood flow [fluorescein angiography (16), indocyanine green angiography (17), Heidelberg Retina Flowmeter (18) and indocyanine green angiography (19), laser Doppler velocimetry and flowmetry (20,21) and laser speckle imaging (22,23)]. The advantage of optical imaging techniques is their remarkably high temporal and spatial resolution. However, the limitations of these techniques are that they require unobstructed light paths, have a small field of view, and cannot resolve signals from different laminar structures (except optical coherence tomography). Consequently, eye diseases, such as senile cataract and

vitreous hemorrhage, often preclude applications of optical retinal imaging techniques. Moreover, blood-flow measurements of the retina have been limited to large surface vessels, which may not accurately reflect local tissue perfusion, and the choroidal vessels are generally inaccessible because they are hidden from view by the retinal pigment epithelium.

MRI

MRI has become a powerful diagnostic tool because it can provide non-invasive anatomical, physiological and functional information in a single setting. Although the spatial resolution of MRI is low compared with that of optical imaging techniques, MRI has no depth limitation, has a large field of view, and is capable of imaging the whole body non-invasively. In the past decade, numerous advances contributed by many laboratories have improved the spatial resolution and contrast of MRI, which is currently capable of visualizing columnar structure and cortical layers in the brain (24–29). These advances have made it possible to explore the possibility of using MRI to visualize anatomy, physiology and function in the retina with laminar-specific resolution.

AIMS OF THIS REVIEW

This paper reviews the recent developments and applications of high-resolution anatomical, physiological (blood flow, blood volume and oxygenation) and functional imaging technologies based on MRI in the retina with layer specificity. It starts by describing the anatomical, blood-oxygenation-level-dependent (BOLD), blood-volume, blood-flow and manganese-enhanced MRI (MEMRI) of normal retinas, followed by applications

of these MRI technologies to investigate two animal models of retinal diseases (retinal degeneration and diabetic retinopathy). MRI offers some unique advantages over existing retinal imaging techniques. In return, the highly structured retina with well-defined layers is an excellent model system for testing and advancing emerging high-resolution, high-contrast anatomical, physiological and functional MRI technologies. These approaches are expected to complement optically based imaging techniques.

A number of studies have begun to explore the potential of MRI for investigating the retina (9,30–44). In this review, we will primarily focus on techniques, methods and results from our laboratory. Additional important topics have been addressed by other contributors to this special issue.

STRUCTURAL MRI

MRI is the method of choice for non-invasive anatomical imaging because of its excellent soft-tissue contrast. The common MRI contrasts are determined by spin density, spin–lattice relaxation time (T_1), spin–spin relaxation time (T_2) and apparent diffusion coefficient (ADC). These contrasts arise from regional differences in water density, macro- and micro-molecular content, ion concentrations and tissue microenvironment, among others. Importantly, these contrasts are often altered in diseases, dependent on disease severity, and specific pathology. Thus, MRI has the potential to detect early disease onset, characterize pathogenesis, and provide improved disease specificity

and, longitudinally monitor disease progression non-invasively *in vivo*.

In addition, the nascent capacity of MRI to distinguish various tissue types in normal and disease states can be further enhanced with exogenous contrast agents. For example, gadolinium diethylenetriaminepenta-acetic acid (GdDTPA) is a biologically stable and non-toxic MRI contrast agent which shortens water T_1 . Normal vessels in the brain and retina are impermeable to GdDTPA because of the presence of the blood–brain and blood–retina barriers, respectively. The retinal vessels consist of non-fenestrated capillaries which are impervious to many tracers, including GdDTPA. In the choroidal circulation, tight junctions between retinal epithelial cells prevent the passage of large molecules (including GdDTPA) from the choriocapillaris (45). Thus, GdDTPA selectively enhances signal in the blood vessels, providing valuable contrast. Moreover, disease-induced changes in vascular permeability (such as brain tumor and stroke) can also be visualized and quantified using GdDTPA-enhanced MRI.

T_1 , T_2 , diffusion-weighted and GdDTPA contrasts

MRI can resolve different anatomical layers in the retina in cats (30,46,47). Multiple ‘layers’ in the retina are observed as alternating bright, dark and bright bands on anatomical images (Fig. 2A, $100 \times 100 \mu\text{m}$). The vitreous and the sclera appear relatively hypointense because the vitreous has a long T_1 and the sclera has low water content and short T_2 .

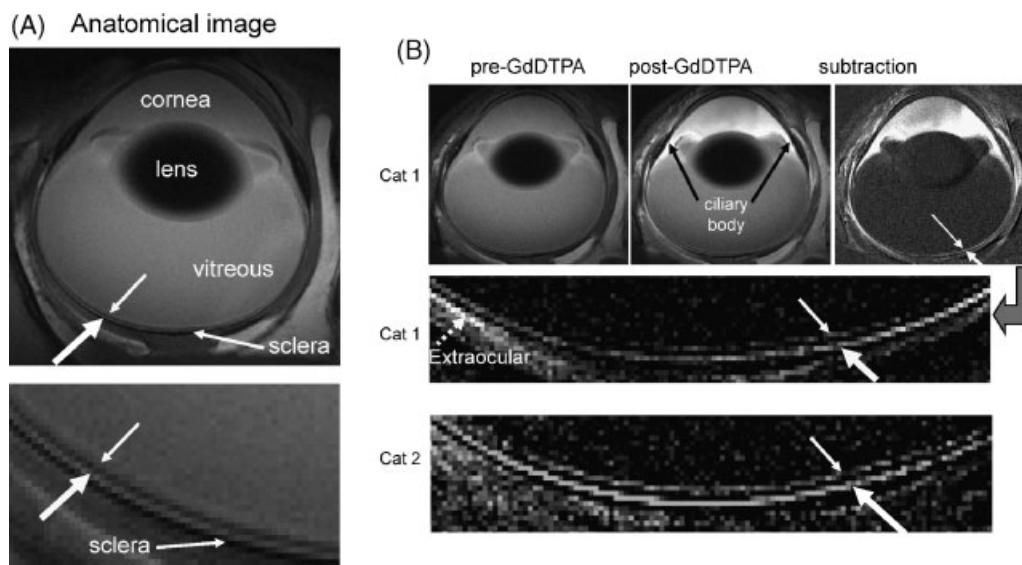


Figure 2. Anatomical and GdDTPA-enhanced MRI of the cat retina. (A) Cross-sectional T_2 -weighted ($TE = 40$ ms) images at $100 \times 100 \times 1500 \mu\text{m}$ resolution. The image slice was obtained at the middle of the eye, roughly bisecting the area centralis. The small and large white arrows indicate the ‘inner’ and ‘outer’ strips, respectively. (B) Contrast-enhanced T_1 -weighted images. The small and large white arrows indicate the ‘inner’ and ‘outer’ bands, respectively. Extraocular enhancement was also observed (dashed arrow). Images were obtained with a custom-made radiofrequency coil placed laterally on the side of the eye. Reproduced from Shen *et al.*, (30), *J Magn Reson Imaging*, with permission.

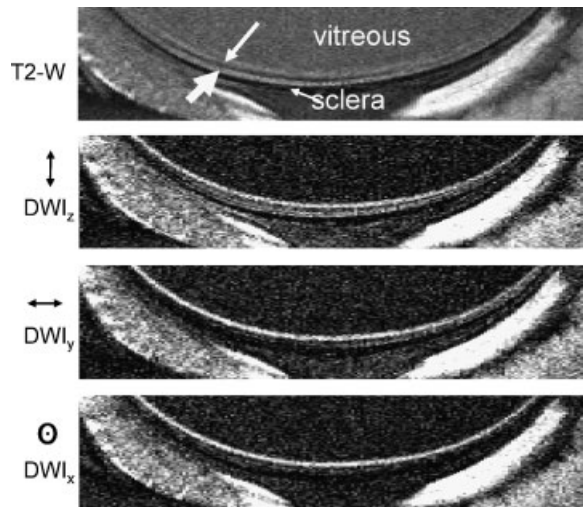


Figure 3. Diffusion-weighted MRI of the cat retina. T_2 -weighted (T_2 -W; $TE = 40$ ms) and diffusion-weighted (DWI; $b = 504$ s/mm²) images at $50 \times 100 \times 1500$ μ m. Diffusion-sensitizing gradients were placed along the x, y or z axis separately. The small and large white arrows indicate the 'inner' and 'outer' strips, respectively. Reproduced from Shen *et al.*, (30), *J Magn Reson Imaging*, with permission.

To corroborate the laminar classification, contrast-enhanced imaging was performed using intravenous GdDTPA (Fig. 2B). GdDTPA enhanced MRI signal on both sides of the retina. Importantly, the outer band was enhanced more and appeared thicker than the inner band. Greater GdDTPA enhancement of the outer band compared with the inner band is consistent with the greater choroidal blood flow and volume than in the retinal vasculature (1,4,5). In contrast, the vitreous and the middle segment of the retina were not enhanced by GdDTPA, consistent with their avascular structures. As expected, enhancement was observed in the extraocular muscles because their blood vessels are permeable to GdDTPA. Similarly, enhancement was observed in the anterior segment of the eye because the ciliary body is permeable to GdDTPA.

In addition, diffusion imaging with diffusion-sensitizing gradients along three principal directions (Fig. 3; 50×100 μ m) revealed diffusion anisotropy in the retina. This is because water displacement in biological tissues is restrictive and anisotropic in the presence of semi-permeable cell membranes and macrostructures. With the diffusion gradient direction perpendicular to the retinal surface at the back of the eye (z axis), alternating bright, dark and bright strips were observed. Three strips on this image co-registered with the three strips on the anatomical images. Layer-specific T_2 and ADC values are summarized in Table 1 (30). The overall T_2 and ADC values of the retina are similar to those of the brain but differ markedly from those of the vitreous and sclera.

To further corroborate the layer-specific resolution of the cat retina, we investigated the rat retina at higher spatial resolution ($60 \times 60 \times 500$ μ m) (9). Adult male Sprague–Dawley rats of 250–350 g were studied. Consistent with the cat data, three distinct 'layers' of alternating bright, dark and bright bands were observed (Fig. 4). Similarly, GdDTPA administration markedly enhanced retinal boundaries, with significantly thicker and more enhanced outer strips than inner strip (Fig. 5) consistent with the greater blood flow in the choroid than in the retinal vasculature. Together, these results confirmed the layer-specific anatomical findings in cats.

Layer assignments and thicknesses

To assign MRI-derived retinal 'layers', images were carefully compared with standard histology. A histological section depicting standard cell layers, the embedded retinal vascular layer and a distinct choroidal vascular layer is shown in Fig. 6. Comparative analysis yielded the following layer assignments. The inner MRI band correlated with the combined GCL and INL with the embedded retinal vessels. Consistent with the inclusion of a vascular component, GdDTPA enhanced this band. The middle band, which appeared relatively hypointense on anatomical imaging, was not enhanced by GdDTPA and

Table 1. Group-average T_2 , $ADC_{//}$ and ADC_{\perp} values of the 'inner', 'middle' and 'outer' strips of the retina, vitreous humor and brain tissues at 4.7 T ($n = 6$, mean \pm SD). Reproduced from Shen *et al.*, (30), *J Magn Reson Imaging*, with permission

		T_2 (ms)	$ADC_{//}$ ($\times 10^{-3}$ mm ² /s)	ADC_{\perp} ($\times 10^{-3}$ mm ² /s)
Retina	Vitreous humor	218 ± 12	2.73 ± 0.22	2.66 ± 0.22
	'inner'	67 ± 5	1.1 ± 0.2	0.74 ± 0.1
	'middle'	48 ± 5	1.2 ± 0.3	0.67 ± 0.1
	'outer'	95 ± 6	3.3 ± 0.7	1.2 ± 0.2
	Muscle around eye ^a	73 ± 8	0.78 ± 0.2	0.75 ± 0.2
	Rat brain gray matter	54 ± 2^b		0.74 ± 0.02^c

^aMuscle at the posterior–dorsal area of the eye was obtained to check for internal consistency.

^bUnpublished rat data ($n = 7$) obtained using essentially identical sequence parameters as herein.

^cAverage ADC measured along x, y and z direction separately from rat brain (132).

*Significant difference ($P < 0.005$). Note: T_2 , $ADC_{//}$ and ADC_{\perp} of the vitreous were significantly different from those of inner, middle and outer strips, except between vitreous and outer strip $ADC_{//}$.

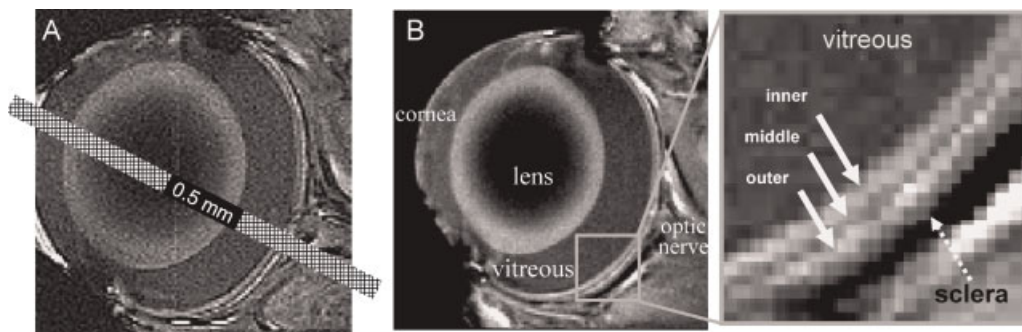


Figure 4. Anatomical MRI of the rat retina. (A) A bar depicting a 0.5 mm-thick MRI slice, overlaid on an edge-enhanced image, illustrating the negligible partial-volume effect due to the retinal curvature. (B) Anatomical images from a normal Sprague–Dawley adult rat retina at $60 \times 60 \times 500 \mu\text{m}$. Three distinct ‘layers’ (solid arrows) of alternating bright, dark and bright bands are evident. Sclera (dashed arrow) is hypointense. Reproduced from Cheng *et al.*, (9), *Proc Natl Acad Sci USA*, with permission.

was thus assigned as the avascular ONL and the photoreceptor segments. GdDTPA enhanced the outer band, which was assigned as the choroidal vascular layer (9).

To quantitatively determine laminar thicknesses, the borders of visualized MRI layers assigned to the retina were detected using an automatic edge-detection technique (Fig. 7). Intensity profiles were projected radially perpendicular to the vitreal–retinal boundary (9). These radial projections were obtained along the length of the retina and averaged into a single intensity profile. The ‘half height’ method (48,49), analogous to common methods for measuring vessel diameters in optical imaging studies, was used to automatically determine band thicknesses. The validity of this approach has been verified by simulation studies (9).

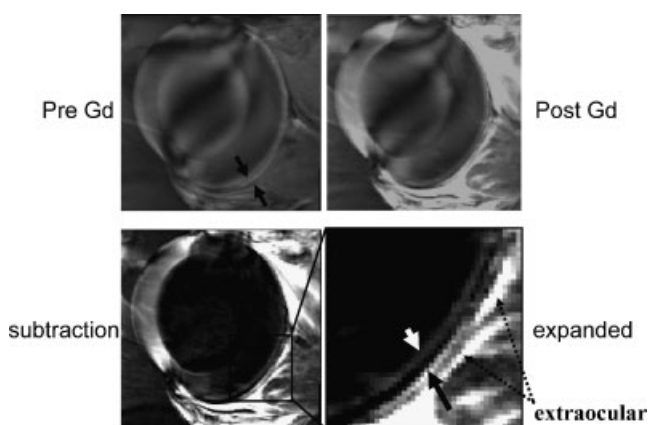


Figure 5. GdDTPA-enhanced MRI of the rat retina. Contrast-enhanced images at $60 \times 60 \times 500 \mu\text{m}$ before and after GdDTPA administration, and the subtracted image. The two arrows in the expanded views indicate the inner and outer bands of the retina corresponding to the two vascular layers, bounding the retina. Two dashed arrows indicate signal enhancement of extraocular tissues supplied by GdDTPA-permeable vessels. Reproduced from Cheng *et al.*, (9), *Proc Natl Acad Sci USA*, with permission.

Reproducibility of repeated layer-specific MRI thickness measurements within the same subjects and across subjects has also been evaluated (9). The inner, middle and outer band thicknesses of the adult Sprague–Dawley rat retina determined by MRI were, respectively, 101 ± 17 , 79 ± 11 , and $86 \pm 10 \mu\text{m}$ (total MRI thickness $267 \pm 31 \mu\text{m}$; mean \pm SD, $n = 24$). The corresponding histological layer thicknesses were $92 \pm 9 \mu\text{m}$ for the innermost layer including the GCL + IPL + INL, $77 \pm 9 \mu\text{m}$ for the central layer including OPL + ONL + OS + IS, and $37 \pm 8 \mu\text{m}$ for the outer layer including choroid (total histological thickness = $205 \pm 11 \mu\text{m}$, $n = 9$). MRI-derived thicknesses of the inner and middle bands were similar to histological measurements ($P > 0.05$), whereas the outer band was significantly thicker than the histology-derived thickness of the choroidal vascular layer ($P < 0.05$). The discrepancy between the *in vivo* and histological measurements of the outer band may arise from the partial-volume effect because of limited MRI spatial resolution, collapse of choroidal vessels after removal of the eyes from systemic circulation, and histological shrinkage, underscoring the importance of *in vivo* measurements.

Interestingly, the total retinal thickness of the cat retina (MRI-derived, $356 \pm 13 \mu\text{m}$ including the choroid; histology-derived, $319 \pm 77 \mu\text{m}$; mean \pm SD) was significantly thicker ($P < 0.05$) than the rat retina ($267 \pm 31 \mu\text{m}$ and $205 \pm 11 \mu\text{m}$, respectively). The greater thickness of the cat retina, measured by MRI, is attributed to its tapetum (Fig. 6), an additional light-reflecting layer that facilitates night vision. The tapetum is vascularized and its MRI contrast is enhanced by intravenously administered GdDTPA. The neural retina in cat was $184 \pm 32 \mu\text{m}$, the tapetum was $86 \pm 35 \mu\text{m}$, and the choroid was $82 \pm 14 \mu\text{m}$ by histology (30). Taken together, these MRI layer assignments are consistent with known cellular and vascular laminar structures of the retina in the two species. MRI studies of mouse (31)

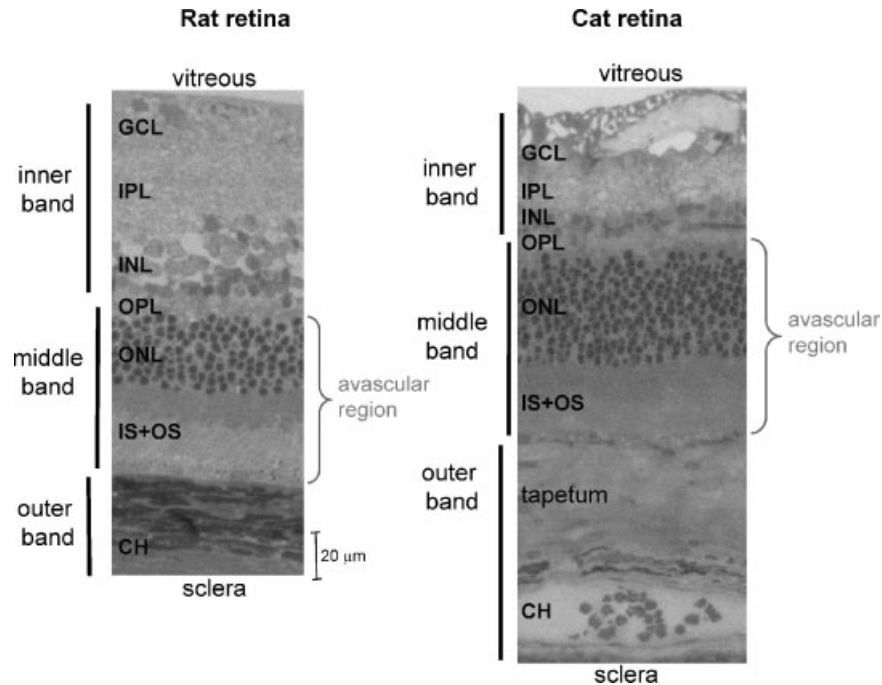


Figure 6. Histology of rat and cat retinas. Histological section of a normal adult Sprague–Dawley rat and cat retina stained with toluidine blue. Three vertical bars on the left show the assignments of the three MRI-derived layers. CH, choroidal vascular layer. In cat, there is an additional layer known as the tapetum, which is vascularized. The rat and cat histological slides are drawn approximately to scale. Adapted and reproduced from Cheng *et al.*, (9), *Proc Natl Acad Sci USA*, and Shen *et al.*, (30), *J Magn Reson Imaging*, with permission.

and rat (37) retinas with layer specificity have also been reported, with similar total retinal thickness in rodents.

BOLD MRI

In the brain, neurovascular coupling of blood flow, blood volume and oxygenation to metabolism and function has been well described for over a century (50). Experimental evidence of such coupling in the retina has only been reported recently. For example, flickering light increases blood flow in the optic nerve head as detected by laser Doppler flowmetry (51,52). Physiological stimulation with oxygen or carbogen modulates tissue oxygenation as measured by oxygen polarographic electrodes (7,53). Visual stimulation modulates optical absorption in the retina as detected by intrinsic optical imaging (22,54,55). Physiologically evoked blood-flow changes in the retina have been detected by laser speckle imaging (22,23). These approaches, however, cannot provide layer-specific mapping information. Retinal anatomy and function are organized in a layer-specific manner, and many retinal diseases affect different retinal layers differently. Thus, layer-specific detection could improve our understanding of pathogenesis and early detection of retinal diseases.

Functional MRI (fMRI) (56) is widely used to non-invasively image brain processes ranging from perception to cognition (57–59), and has made remarkable contri-

bution to many scientific disciplines. The most widely used fMRI technique is based on the BOLD signal (56). BOLD contrast originates from the intravoxel magnetic field inhomogeneity induced by paramagnetic deoxyhemoglobin in red blood cells. Changes in regional deoxyhemoglobin content can be visualized in susceptibility-sensitized BOLD images. When a task is performed, regional blood flow to specific brain areas increases, enhancing oxygen delivery beyond the stimulus-evoked increase in oxygen consumption needed to fuel elevated neural activity. The net increase in delivered oxygenated blood produces a regional reduction in deoxyhemoglobin concentration and is detected as an increase in BOLD signal relative to baseline conditions. Therefore, BOLD fMRI provides sensitive and non-invasive visualization of dynamic brain activity in real time. It is important to note that BOLD fMRI does not measure neural activity directly; rather, it detects hemodynamic and metabolic changes associated with increased neural activity. Therefore, assessment of ‘function’ is derived from hemodynamic–metabolic coupling, which has been correlated with evoked field potentials (60). Similarly, stimulus-evoked changes in blood flow and blood volume can also be measured. Although blood-flow and blood-volume fMRI generally have poorer sensitivity per unit time, they are more spatially specific to the site of ‘activations’ (61) and easier to interpret because these two techniques measure single

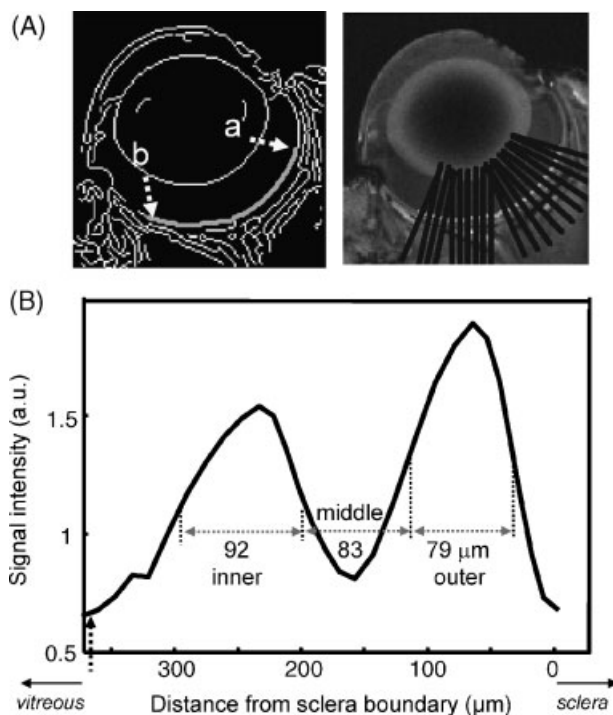


Figure 7. Automated analysis of layer-specific retinal thickness. (A) The retina was segmented using an edge-detection technique. Retinal thickness was quantified from point *a* to *b*, cognizant of some irregular retinal thickness from posterior pole to the pars plana. (B) Intensity profiles of a animal delineates the outer, middle and inner bands. The vertical dashed arrows indicate the vitreous boundary. Values in μm indicate the band thicknesses. Reproduced from Cheng *et al.*, (9), *Proc Natl Acad Sci USA*, with permission.

physiological parameters, in contrast with the BOLD fMRI technique which is a convolution of changes in blood flow, oxygenation metabolism and biophysical parameters (61).

BOLD fMRI techniques have also been extensively utilized to study neurovascular coupling (neurovascular reactivity) in the brain associated with physiological (such as hyperoxic and mild hypercapnic) challenges (62–65). These physiological stimuli modulate cerebral blood flow, blood volume and oxygenation without changing neural activity, providing valuable information about the integrity of neurovascular coupling, independent of changes in neural activity in normal and diseased brain.

We used high-resolution BOLD physiological fMRI to study retinal neurovascular coupling using hyperoxic (100% O_2) and hypercapnic (5% CO_2 + 21% O_2) challenges with air as the baseline (9). Spin-echo echo-planar imaging at $90 \times 90 \mu\text{m}$ was implemented with diffusion weighting to suppress the strong vitreous signals. Layer-specific physiological fMRI responses were detected using BOLD fMRI (Fig. 8). Importantly, the two vascular layers in the retina responded differently to the inhalation

stimuli, indicating differential blood-flow regulation. To objectively analyze the layer-specific BOLD physiological fMRI data and minimize the partial-volume effect, three equal regions of interest were automatically prescribed for the three 'bands'. The outer and inner probably predominantly included the choroidal and retinal vascular layers.

Hyperoxic challenge

Hyperoxia induced a larger BOLD response in the outer band ($12 \pm 2\%$, mean \pm SD, $n = 8$) than in the inner band ($7 \pm 2\%$, $P < 0.01$). We interpret this as being due to increased capillary and venous oxygen saturation, thus increased BOLD signal relative to baseline (56). Interestingly, the arteriovenous oxygen difference in the choroid is small compared with the brain (1,4,5), and thus one might expect a correspondingly smaller hyperoxia-induced increase in BOLD signal in the choroid. However, our hyperoxia-induced BOLD data showed a larger increase in the outer band (choroidal vascular layer) than in the inner band (retinal vascular layer). This is probably because hyperoxia is known to vasoconstrict retinal vessels and thus markedly decrease retinal blood flow by as much as 60% (20,66) [compared with typical 13% in the brain (67)], which counteracts the BOLD signal increase from elevated oxygen tension by hyperoxia *per se* in the retinal vessels. In contrast, hyperoxia does not significantly vasoconstrict choroidal vessels and thus does not significantly affect choroidal blood flow (20,66). Thus, the BOLD signal increase in the inner band containing the retinal vessels was smaller than in the outer band containing the choroidal vessels. The higher choroidal vascular density in the outer band and the lower retinal vascular density in the inner band may further amplify the differential BOLD responses between the two vasculatures.

Hypercapnic challenge

In contrast with hyperoxia, hypercapnia induced a smaller BOLD response in the outer band ($1.6 \pm 1\%$; mean \pm SD, $n = 8$) than in the inner band ($10 \pm 2\%$, $P < 0.01$). This is because CO_2 inhalation increases blood flow from vasodilation, resulting in decreased fractional oxygen extraction and increased capillary and venous oxygen saturation, and thus increases BOLD signal relative to baseline (56). In the retina, hypercapnia strongly vasodilates retinal vessels, whereas it has a smaller vasodilatory effect on choroidal blood vessels (5,66). The reduced choroidal vasodilation is probably due to unique choroidal physiology or a 'ceiling effect' as the result of high basal choroidal blood flow (64). Thus, the BOLD signal increase in the inner band containing the retinal vessels was larger than in the outer band containing the choroidal vessels.

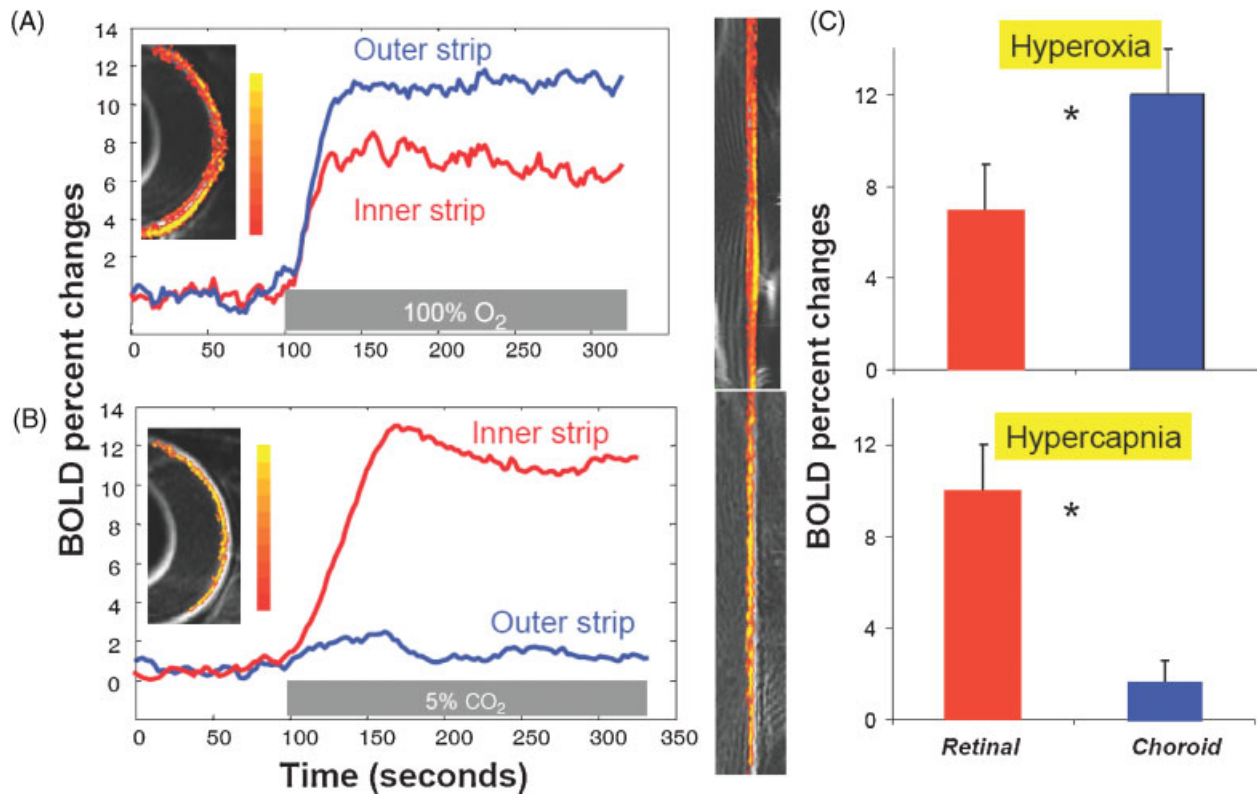


Figure 8. BOLD fMRI response of the retina. Lamina-specific BOLD fMRI responses to (A) hyperoxia (100% O₂) and (B) hypercapnia (5% CO₂ in air) from a normal rat at 90 × 90 × 1000 μm in-plane resolution. BOLD percentage change maps are overlaid on echo-planar images. The color bar indicates BOLD percentage changes. (C) Group-averaged hyperoxia- and hypercapnia-induced BOLD percentage change in the inner and outer strip (mean ± SD, n = 8). Note that these percentage changes due to either hyperoxic or hypercapnic stimulation are larger than those typically reported in the brain, probably because of a greater vascular density in the retina. Reproduced from Cheng *et al.*, (9), *Proc Natl Acad Sci USA*, with permission.

In sum, the BOLD physiological fMRI responses in the two vascular layers enable further investigation of retinal physiology, allowing segregation of layer-specific effects. These hyperoxic and hypercapnic results support the contention that the two vascular supplies to the retina are differentially regulated. These differential responses are consistent with oxygen-electrode (53) and laser Doppler velocimetry (68) measurements. Laser Doppler velocimetry can only measure blood flow in the optic nerve head, or choroidal blood flow in the human fovea, where retinal vessels are absent. Finally, we note that the BOLD signal source is a complicated convolution of changes in blood flow, blood volume and other biophysical parameters (29,69). More direct layer-specific MRI measurement of blood volume and blood flow could confirm these layer-specific BOLD physiological fMRI findings.

MRI has also been used to document oxygenation changes in the vitreous adjacent to the retina using the ΔP_{O₂} technique (36). The ΔP_{O₂} signal contrast is based on dissolved molecular O₂, a weak paramagnetic relaxation agent. Vitreal oxygenation changes have been shown to be sensitive to carbogen breathing (95% O₂ + 5% CO₂) relative to air, and vitreal oxygenation

changes have been reported in normal and diabetic rats (38) and humans (40).

BLOOD-FLOW MRI

To further corroborate the BOLD and blood-volume findings, blood-flow MRI and physiological fMRI were measured. Blood flow can be directly imaged by MRI using: (i) the dynamic susceptibility contrast technique with a bolus of an exogenous intravascular contrast agent or (ii) the arterial spin-labeling (ASL) technique in which the endogenous water in the in-flowing blood is magnetically labeled non-invasively (70). These blood-flow methods (71–76) are established and have been extensively cross-validated with autoradiography (77) and positron emission tomography in the brain (78,79). Importantly, the ASL technique permits repeated measurements, which can be used to dynamically monitor blood flow in real time. This can be used to monitor changes associated with stimuli (i.e. fMRI), to improve signal-to-noise ratio and spatial resolution (70). ASL offers an advantage over dynamic susceptibility contrast

MRI, which can only be performed once because of recirculation of the long intravascular half-life contrast agent, which generally precludes it from use for very high-resolution blood-flow measurement which requires signal averaging. Moreover, ASL blood-flow fMRI can be tailored to be more sensitive to blood flow in smaller vessels, which better reflects local tissue perfusion, and is more spatially specific to sites of increased neural activity compared with the BOLD fMRI signal, which is susceptible to 'draining vein' contamination (27). The key challenge is that the signal-to-noise ratio of blood-flow MRI is two orders of magnitude lower than that of the typical anatomical and BOLD MRI because the blood volume in the brain is only 3–5% of total tissue volume. Blood volume in the retina is probably similar to that in the brain. Nonetheless, blood-flow MRI has the sensitivity and specificity to resolve cortical columns in the brain (27). Basal blood flow and stimulus-evoked and pathology-induced blood-flow changes have been well described in the brain (70–76,80–82). However, blood-flow MRI application in the retina requires significantly higher spatial resolution.

Basal blood flow

We implemented the ASL technique with a separate neck labeling coil and snap-shot gradient echo-planar imaging to measure quantitative blood flow in the rat retina ($90 \times 90 \mu\text{m}$) (83). The butterfly neck coil was placed at the position of the common carotid arteries for ASL. The neck and the eye coils are actively decoupled (83). Blood-flow signals (S_{BF}) in mL/g/min are calculated pixel-by-pixel using $S_{\text{BF}} = \lambda/T_1 [(S_{\text{C}} - S_{\text{L}})/(S_{\text{L}} + (2\alpha - 1) S_{\text{C}})]$ (83), where S_{C} and S_{L} are signal intensities of the non-labeled and labeled images, respectively, λ , the water tissue–blood partition coefficient, is 0.9 (84), T_1 is 1.7 s at 7 T, and α , the ASL efficiency, is 0.8 (83). Quantitative basal blood-flow images at $90 \times 90 \mu\text{m}$ showed excellent contrast in the rat retina and the ciliary body, whereas blood flow in the lens, cornea and vitreous were within noise level (Fig. 9A) (34). Blood flow was confirmed as the source of the signals by repeating measurements after the animals had been sacrificed in the scanner, revealing no statistically significant blood-flow contrast in the post-mortem retina (mean 0.03 ± 0.01 mL/g/min, $n = 3$). Blood flow was relatively constant along the length of the retina as a function of distance from the optic nerve head (Fig. 9B), except that it fell significantly at the distal edges where the retina terminates, as expected. The whole-retina blood flow was 6.3 ± 1.0 mL/g/min (mean \pm SD, $n = 6$) under 1.1% isoflurane, remarkably higher than previous measurements of cerebral blood flow of 0.9 ± 0.13 mL/g/min (85) and 1.1 ± 0.04 mL/g/min (64) under essentially identical experimental conditions. These findings are consistent with blood flow in the retina and brain obtained in the same animals using microsphere techniques (86,87). The current spatial resolution of

blood-flow MRI is insufficient to resolve the two vascular layers, and the measured value is in between the retinal and choroidal blood flow. Improving resolution and sensitivity to resolve the two vascular layers and the avascular layer is under investigation.

Hyperoxic and hypercapnic challenge

In addition, we also investigated blood-flow responses to physiological challenge in the retina. Physiological stimuli evoked robust blood-flow changes in the retina. Hyperoxia decreased blood flow, whereas hypercapnia increased blood flow relative to air (Fig. 10A) (34). Group-averaged blood-flow profiles across the retinal thickness (from sclera to vitreous) before and during physiological challenges are shown in Fig. 10B.

To further demonstrate the sensitivity of this technique, measurements were also made at two different isoflurane concentrations in air. Blood flow in the retina increased from 6.3 ± 1.0 mL/g/min (mean \pm SD, $n = 6$) under 1.1% isoflurane to 9.3 ± 2.7 mL/g/min (mean \pm SD, $n = 6$) under 1.5% isoflurane ($P < 0.05$) (34). Isoflurane is a known potent vasodilator in the brain (88), where cerebral blood flow under 1.1% isoflurane (1.27 ± 0.29 mL/g/min) was higher than in awake restrained conditions (0.86 ± 0.25 mL/g/min) in the same animals (89). Increasing isoflurane concentration from 1% to 2% increased cerebral blood flow from 0.87 ± 0.27 to 1.31 ± 0.30 mL/g/min in the same animals (90). Our retinal blood-flow results suggest that isoflurane has an overall stronger vasodilatory effect on vessels in the retina than in the brain. The effects of isoflurane on retinal and choroidal vessels remain to be investigated.

In sum, these data demonstrate a proof of principle that quantitative basal blood flow in the retina and its responses to physiological stimuli can be reliably imaged using non-invasive, high-resolution MRI without depth limitation. Alteration of blood flow is involved or contributes to the pathogenesis of many retinal diseases and, thus, blood-flow measurements of the retina may provide important clinically relevant information. Importantly, the quantitative nature of blood-flow MRI will allow comparisons among different experimental groups and is well suited for longitudinal monitoring of disease progression. Improving spatial resolution to resolve blood flow in the retinal and choroidal vasculature is currently under investigation.

FMRI OF VISUAL STIMULATION

Visual stimulation

BOLD fMRI has been successfully used to detect retinal responses to visual stimulation in cats, but at insufficient spatial resolution to probe layer specificity (91). Visual

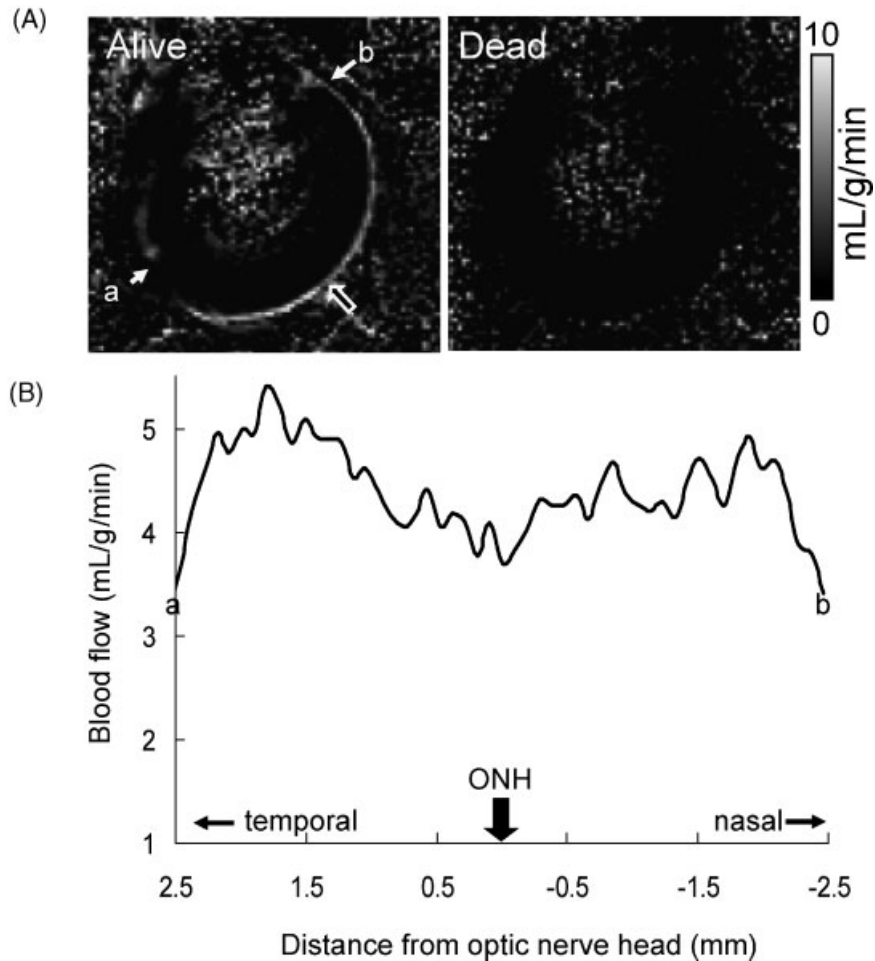


Figure 9. Basal blood-flow image of the retina. (A) Quantitative basal blood-flow images were obtained from an alive and dead animal (same animal). Blood-flow values in the retina and the ciliary body are high, whereas blood flow in the lens and vitreous are within noise levels. Large arrows indicate the locations of the optic nerve head (ONH). (B) Blood-flow values as a function of distance from the ONH. Data were obtained from one distal edge to another (point a to b). Reproduced from Li *et al.*, (34), *Neuro image*, with permission.

stimuli using drifting gratings with dark as the basal condition were presented to an upper or lower quadrant of the visual field in anesthetized cats. As expected, a stimulus presented in the upper half of the visual field stimulated the lower part of the retina, whereas stimulus presented in the lower half of the visual field stimulated the upper part of the retina evident in spatially distinct retinal changes in the BOLD fMRI signal (Fig. 11A).

Stationary versus drifting gratings

To gauge the BOLD fMRI sensitivity, we investigated drifting and stationary gratings with identical contrast and luminance relative to dark as the basal condition (Fig. 11B) (91). Although both drifting and stationary gratings evoked increased BOLD fMRI signals relative to the dark condition, signal change associated with the drifting gratings ($2.0 \pm 0.3\%$, mean \pm SD, $n = 2$, four

measurements) were twice that associated with stationary gratings ($1.0 \pm 0.1\%$) ($P < 0.02$), demonstrating the sensitivity of BOLD fMRI to detect small differences between stationary and drifting gratings of the same luminance. Future studies will focus on resolving layer-specific blood-flow, blood-volume and BOLD fMRI responses to cell-type-selective visual stimuli.

MEMRI

MEMRI

Manganese (Mn) is both an MRI contrast agent and a calcium analog. Unlike calcium, Mn is trapped in the intracellular space with a half-life of a few days (92,93), and thus selectively enhances intracellular water MRI signals. MEMRI (76,94) has been used to map increased calcium-dependent neural activity, independent of hemo-

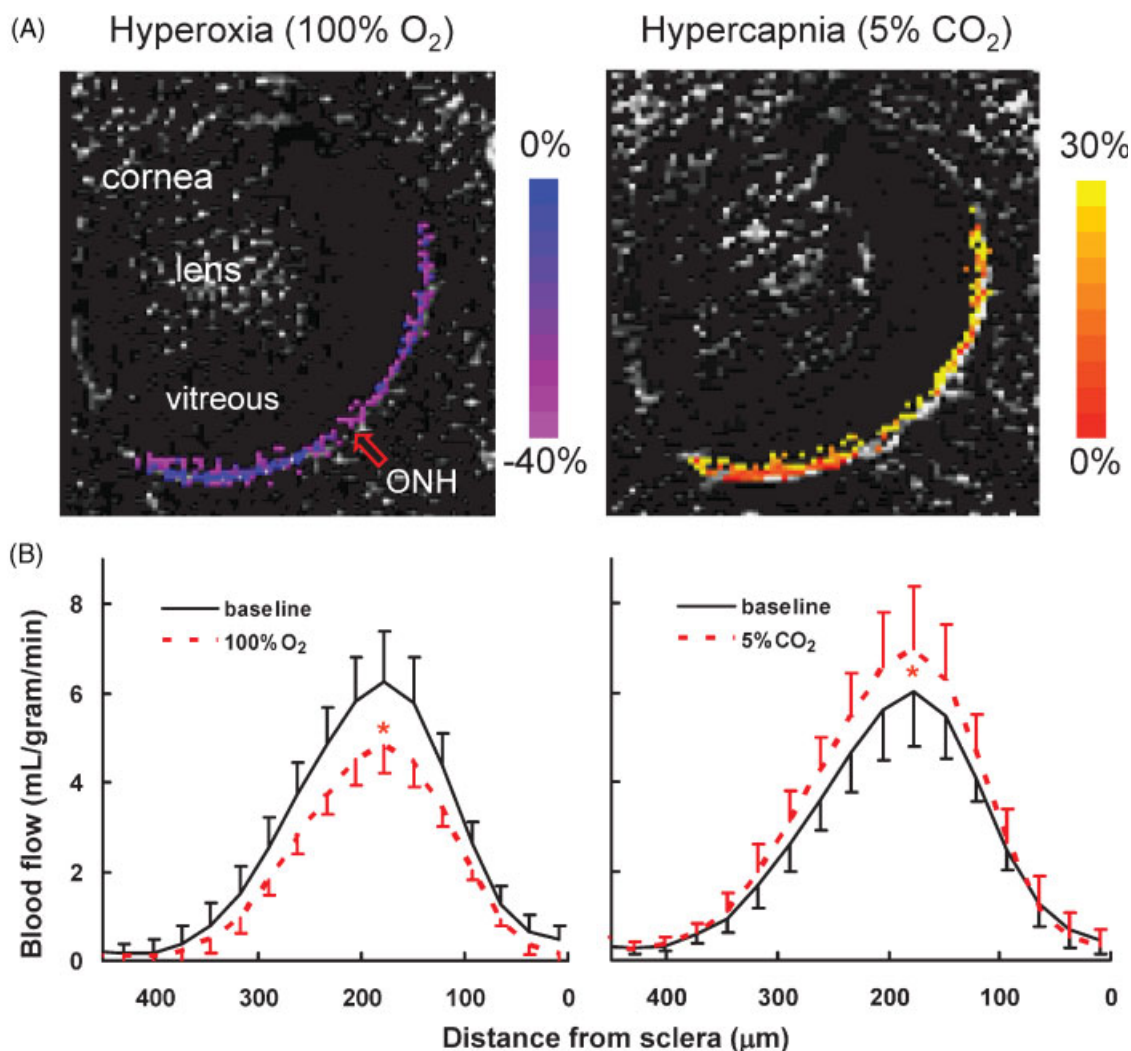


Figure 10. Physiologically induced blood-flow changes in the retina. (A) Blood flow percentage change maps responding to physiological stimuli (100% O₂ or 5% CO₂) obtained from a representative animal. Percentage changes are overlaid on blood flow maps. Color bars indicate blood-flow percentage changes. ONH, optic nerve head. (B) Group-averaged blood-flow profiles across the retinal thickness (mean \pm SD, $n = 5$) under basal conditions, 5% CO₂ or 100% O₂. Blood-flow changes due to hyperoxia and hypercapnia were significantly different from baseline (air) ($P < 0.05$). Reproduced from Li *et al.*, (34), *Neuroimage*, with permission.

dynamic changes, and to track *in vivo* white-matter fiber connectivity because Mn can be packaged, released and transported across synapses like calcium (95). MEMRI application is expanding rapidly. Recent reports include somatosensory and pharmacological stimuli, stroke with perturbed Mn uptakes, and white-matter diseases with perturbed Mn synaptic transport in the brain [see reviews (96,97)]. MEMRI has also exploited regional differences in basal calcium activity in the brain to improve anatomical contrast (98,99).

We explored the use of MEMRI to improve anatomical contrast among retinal layers (33). MnCl₂ was injected directly into the vitreous and imaged at 25 \times 25 μ m in-plane resolution 24 h after injection. High-contrast MEMRI of normal retinas revealed seven distinct bands of alternating hyper- and hypo-intensities (Fig. 12). The

signal intensity profiles across the retinal thickness showed a diffuse bright band closest to the vitreous (#1) and three bright bands (#3, #5 and #7) interspersed among three dark bands (#2, #4 and #6). To confirm vascular layer boundaries, GdDTPA was injected intravenously into the same animal. GdDTPA enhancement was consistently seen in retinal layers 1–3 and in layer 7 but not in the sclera, vitreous or in retinal layers 4–6.

Layer assignments

Taken together, these results suggest that the brighter bands are associated with cell bodies, whereas the darker bands are associated with plexiform (synaptic) and photoreceptor segment layers. We tentatively assigned

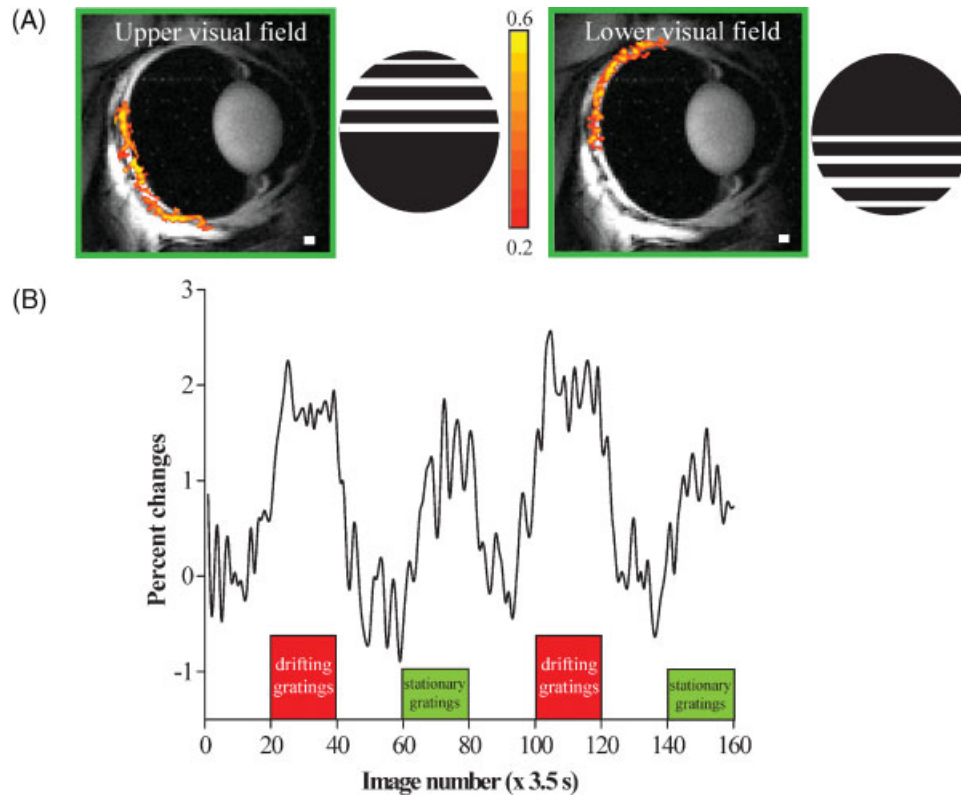


Figure 11. fMRI of visual stimulation of the cat retina. (A) fMRI maps ($468 \times 468 \times 1000 \mu\text{m}$) of the upper and lower visual field using drifting gratings versus dark. The gratings were square wave with 0.15 cycle/degree and 2 cycles/s. The color bar indicates the cross-correlation coefficient. (B) fMRI signal modulation under dark, drifting gratings and stationary gratings (same luminance). Positive signal changes are observed under both drifting-grating and stationary-grating stimuli relative to the dark basal conditions. Signal change due to the drifting gratings is approximately twice that due to stationary gratings. Adapted from Duong *et al.*, (91), *Invest Ophthalmol Vis Sci*.

(33) bands 1–3 in MEMRI as the GCL, IPL and INL, respectively. These bands were also enhanced by GdDTPA, consistent with known vascularity. Bands 4–6 were tentatively assigned as the OPL, ONL, and IS + OS. These bands were not significantly enhanced by GdDTPA, although the partial-volume effect may limit resolution. Band 7 was heavily enhanced by Mn, consistent with Mn accumulation in the endothelial cells lining the choroidal vessels that form the blood–retinal barrier, similar to Mn accumulation in the brain attributed to the cerebral vascular endothelium (76,94). Band 7 was further and strongly enhanced by GdDTPA, confirming its vascularity, and was assigned as the choroidal vascular layer. Direct validation of these layer assignments are under investigation.

MEMRI of the retina after intraperitoneal Mn administration has also been reported to reveal three, as opposed to seven, distinct retinal layers (37). This approach was also used to visualize differences in MEMRI accumulation between prolonged light and dark adaptation (41) and between normal and ocular injury or diseases (42,43), including glaucoma (100).

APPLICATIONS TO RETINAL DISEASES

As illustrated in the data presented above, MRI applied to the retina is a powerful technique for non-invasively obtaining anatomical, functional, blood-flow, and blood-volume data on the retina. These non-invasive imaging technologies could enable longitudinal staging of diseases and testing of therapeutic interventions, and ultimately improve our understanding of disease processes *in vivo*. As an example of potential disease applications, we used these MRI technologies to investigate two retinal diseases that represent leading causes of blindness: retinitis pigmentosa and diabetic retinopathy.

Retinitis pigmentosa

Retinitis pigmentosa is a family of hereditary photoreceptor degenerative diseases characterized by progressive loss of vision and affecting about 1.5 million people world wide (101). Over 150 different gene

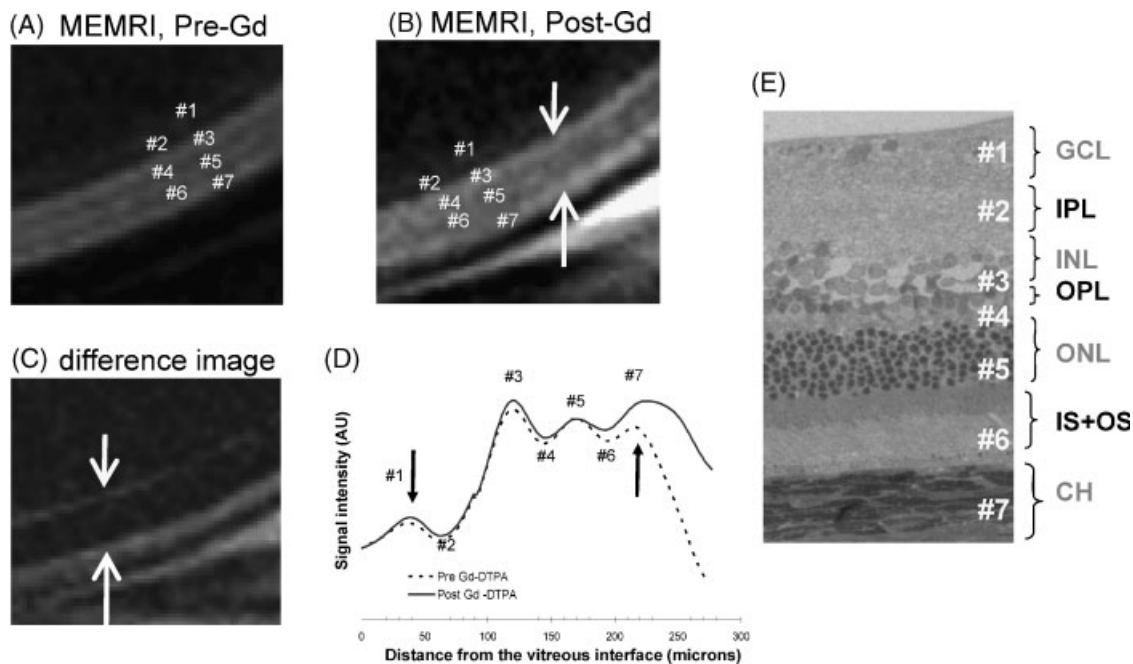


Figure 12. MEMRI. T_1 -weighted images at $25 \times 25 \times 800 \mu\text{m}$ of a rat intravitreally injected with MnCl_2 ~ 24 h earlier (A) before, (B) after GdDTPA intravenous administration and (C) the 'difference' image. MEMRI reveals seven distinct layers of alternative bright and dark contrasts. GdDTPA further enhanced the outer bands on either side of the retina (as indicated by arrows). (D) Signal intensity profiles obtained across the thickness of the retina before and after the intravenous administration of GdDTPA. (E) Histological section of a normal adult Sprague-Dawley rat stained with toluidine blue. The tentative MRI layer assignments are: GCL, IPL, INL, OPL, ONL, photoreceptor inner and outer segments (IS + OS), and choroid (CH). This figure appeared previously in abstract form (33).

mutations are known to cause progressive photoreceptor degeneration (<http://www.sph.uth.tmc.edu/Retnet>). Evaluation of emerging treatments intended to slow or reverse retinal degeneration, including vitamin A supplementation, intravitreal administration of growth factors (102) and neuroprotective drugs (103), gene therapy (104), and prosthetics (105) would benefit from *in vivo* monitoring of the disease.

The Royal College of Surgeons (RCS) rat (106) is an animal model that shares a mutation in the *Merk* gene with many patients with retinitis pigmentosa (107). This mutation results in impaired phagocytosis of the shed photoreceptor outer segment by the retinal pigment epithelium (108). The RCS rat retina begins to degenerate ~ 20 days after birth (P20) and is complete by P90 (53,109). Although RCS rat retinas have been well characterized genetically (107) and histologically (110,111), the lack of non-invasive physiological imaging techniques limits the investigation of the physiological and functional changes and temporal progression *in vivo*.

We compared retinas of RCS rats by MRI at P16 and P120, representing stages before and after degeneration (9). At P16, three distinct layers were visible, confirming normal retinal morphology (Fig. 13). However, at P120 only a single band was visible. Intravenous GdDTPA

administration enhanced the entire retinal thickness in the P120 RCS rat, consistent with the loss of the avascular ONL and IS + OS. Intensity profiles revealed an absent middle band and an overall thinning of the P120 retina. Interestingly, the outer band appeared slightly thickened. The loss of photoreceptor layers and thinning of retinal thickness was confirmed in histological sections of the same retinas (9). These results are summarized in Table 2. Note that the retinas at P16 are thicker than adult retinas (total thickness determined by MRI, $267 \pm 31 \mu\text{m}$, $n = 24$, and by histology $205 \pm 11 \mu\text{m}$, $n = 9$, mean \pm SD), suggesting an age-dependent effect.

BOLD fMRI associated with hyperoxia and hypercapnia was also performed on P120 RCS rats. BOLD fMRI changes in response to hyperoxia in P120 were detected in both retinal and choroidal vascular layers (inner band, $4.2 \pm 2.5\%$; outer band, $8.7 \pm 2.4\%$; mean \pm SD, $n = 4$). However, they were significantly smaller than those of control animals ($7 \pm 2\%$ and $12 \pm 2\%$, respectively; mean \pm SD, $n = 8$). In response to hypercapnia, BOLD fMRI responses largely disappeared from P120 RCS rat retinas (inner band, $-0.02 \pm 6.5\%$; outer band, $0.003 \pm 6\%$; mean \pm SD, $n = 4$), in contrast with those of control animals ($10 \pm 2\%$ and $1.6 \pm 1\%$, respectively; mean \pm SD, $n = 8$). Diminished BOLD response in the choroidal vasculature is perhaps not

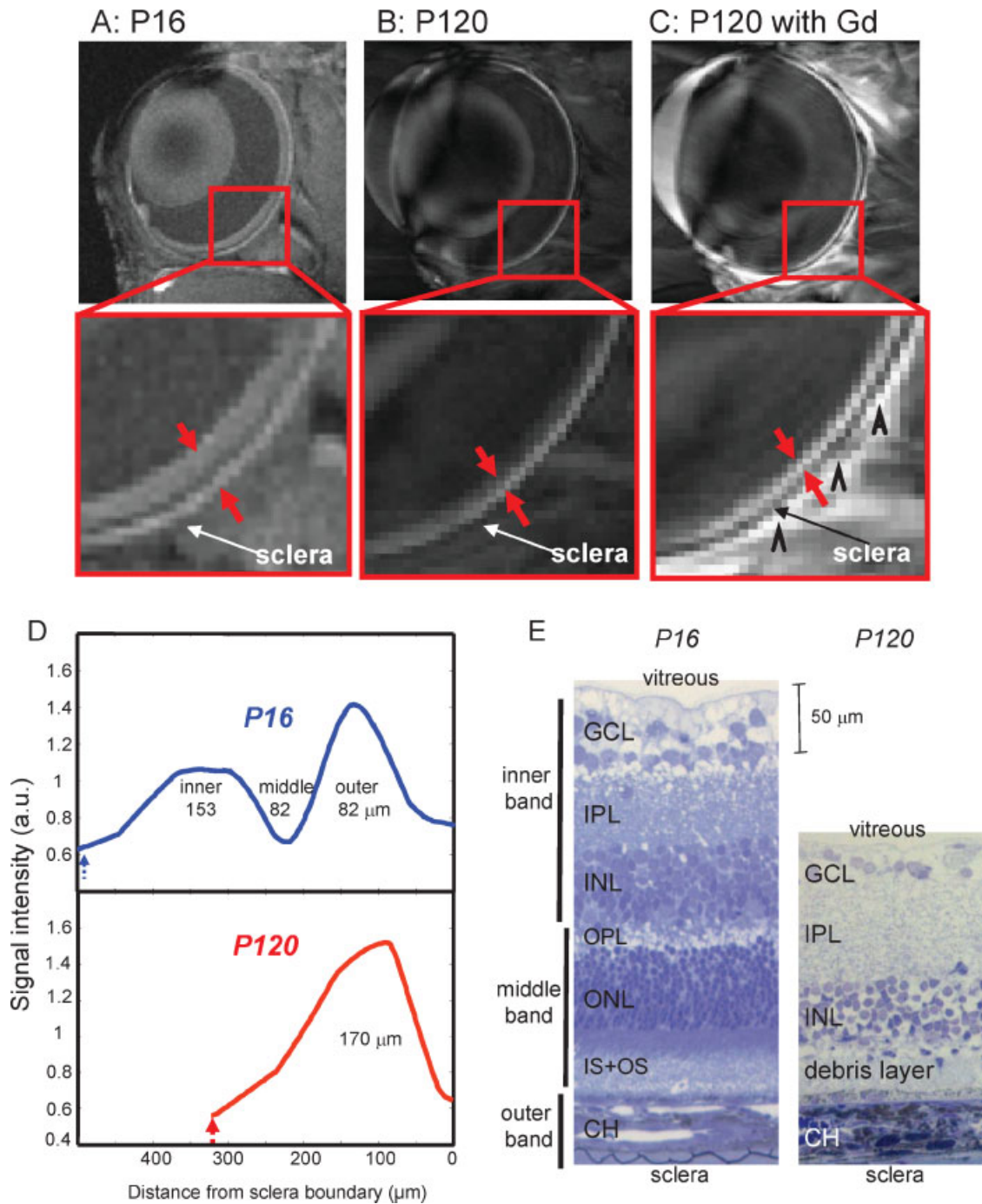


Figure 13. Anatomical MRI of retinal degeneration in RCS rat retinas. Anatomical images at $60 \times 60 \times 500 \mu\text{m}$ of (A) P16 RCS rat retina before photoreceptor degeneration (control), and degenerated P120 RCS rat retina (B) before and (C) after intravenous administration of GdDTPA. Arrowheads in (C) indicate signal enhancement of extraocular tissues. Intensity profiles (D) and histological sections (E) show thinning of the P120 compared with the P16 RCS rat retina. The vertical dashed arrows in (D) indicate the vitreous boundaries. Reproduced from Cheng *et al.*, (9), *Proc Natl Acad Sci USA*, with permission.

surprising, as the choroidal vasculature supplies predominantly the ONL, which has degenerated by P120 in the RCS rat. The reduced BOLD response in the retinal vascular layer may be a secondary effect of photoreceptor degeneration (i.e. thinning of the inner retina). The observed structural changes are consistent with perturbed

neural–vascular coupling, as evidenced by abnormal RCS rat retinal oxygen profiles under basal conditions (53). Perturbed retinal circulation has also been reported in human retinitis pigmentosa (112). We know of no publication describing laser Doppler flow or intrinsic optical imaging physiologically evoked or stimulus-

Table 2. Layer thicknesses (μm , mean \pm SD) of P16 and P120 RCS rat retinas (Long Evans rats). Reproduced from Cheng et al., (9), *Proc Natl Acad Sci USA*, with permission

	P16		P120	
	MRI (n = 6)	Histology (n = 5)	MRI (n = 4)	Histology (n = 4)
Inner band	157 \pm 6	167 \pm 31*	—	101 \pm 21*
Middle band	99 \pm 17	112 \pm 20	—	29 \pm 8
Outer band	95 \pm 15**	34 \pm 4**	—	35 \pm 1
Total	350 \pm 13	307 \pm 41	169 \pm 13	169 \pm 23

*, ** $P < 0.05$, indicating the corresponding comparison.

evoked changes in RCS rat retinas. Blood-flow perturbation associated with retinal degeneration has also been reported recently in a conference abstract (113).

In brief, non-invasive imaging technologies that can pinpoint layer-specific cellular and vascular changes would enable longitudinal staging of the disease, accurate testing of therapeutic interventions, and improved understanding of disease processes *in vivo*. In turn, the RCS rat retina with progressive degeneration of the outer retinal layers can help in MRI retinal layer assignments and thus offers an ideal model for testing emerging high-resolution MRI technologies.

Diabetic retinopathy

Diabetic retinopathy is the leading cause of blindness for people between the ages of 20 and 74 (114). Vision loss from diabetic retinopathy is preceded by vascular perturbations including thickening of the vascular layer, altered vascular autoregulation, enhanced permeability, and vascular occlusion (115–118). Insufficient oxygen delivery causing retinal hypoxia is believed to lead to proliferative diabetic retinopathy (119–121), although direct evidence is lacking. Laser panretinal photocoagulation, the most established treatment for diabetic retinopathy, limits proliferative neovascularization and prevents vision loss, but sacrifices the retina (114). Consequently, laser panretinal photocoagulation is indicated only after diabetic retinopathy is firmly established. Laser panretinal photocoagulation is thought to reduce photoreceptor oxygen consumption, allowing choroid-derived oxygen to reach the inner retina and reduce inner retinal hypoxia, which reduces neovascularization (119,120,122–125). Less destructive interventions, applicable at earlier pathogenic time points, are desirable. However, diagnostic criteria for diabetic retinopathy before the establishment of vascular dysfunction do not yet exist. Despite intense efforts, studies have failed to identify a single clinically significant parameter

that predicts the development of diabetic retinopathy (115,126–129). Consequently, investigative modalities with the potential to evaluate structural and functional attributes of retinas are needed. In this context, retinal MRI may provide critical data.

To demonstrate the feasibility of MRI to detect diabetic retinopathy changes before the development of late-stage vasculopathy, we compared rat retinas after 3 months of streptozotocin (STZ)-induced hyperglycemia with age-matched, non-diabetic controls (130). Male Sprague–Dawley rats (200–250 g) were made diabetic by intravenous injections of streptozotocin (100 mg/kg). Diabetes was defined as two successive daily random blood glucose values >200 mg/dL. Random blood glucose measurements were performed twice a week using a hand-held blood glucose monitor. Small doses of insulin were provided to prevent weight loss, but maintain hyperglycemia. Insulin was administered by subcutaneously implanted continuous-release pellets (Linplant; LinShin, Scarborough, ON, Canada), composed of microcrystallized palmitic acid and bovine insulin. MRI showed that the inner and middle layer thicknesses (Table 3), constituting the neural retina, remained unchanged in diabetic retinas 3 months after STZ injection. Interestingly, the outer ‘choroid’ layer thickness increased in diabetic retinopathy. We are not aware of any report on choroidal vascular layer thickness of diabetic retinopathy *in vivo*. Histological analysis of choroidal thickness is susceptible to artifact, as the extracted retina often detaches at the retinal pigment epithelium, excluding the choroid. Further, choroidal blood vessels collapse once dissociated from systemic blood flow. These findings underscore the potential for retinal MRI for longitudinally monitoring early changes in the progression of diabetic retinopathy.

In addition, we used BOLD fMRI to compare retinal blood oxygenation during early diabetic retinopathy in response to changes in inhaled gases 3 months after STZ injection when vascular changes are not readily apparent in rats. STZ-diabetic and control rats were ventilated sequentially with 100% O₂ to induce hyperoxia, or 5% CO₂ to induce hypercapnia, relative to air as the baseline. Our preliminary analysis found that, although

Table 3. MRI retinal thickness of diabetic retina 14 weeks of hyperglycemia and in non-diabetic controls (n = 4 each). Reproduced from Cheng et al., (9), *Proc Natl Acad Sci USA*, and Shen et al., (30), *J Magn Reson Imaging*, with permission

	Control	Retinopathy
Inner layer	107 \pm 16	114 \pm 23
Middle layer	84 \pm 10	86 \pm 14
Outer layer	87 \pm 10*	103 \pm 23*
Total	278 \pm 28	303 \pm 55

* $P < 0.05$.

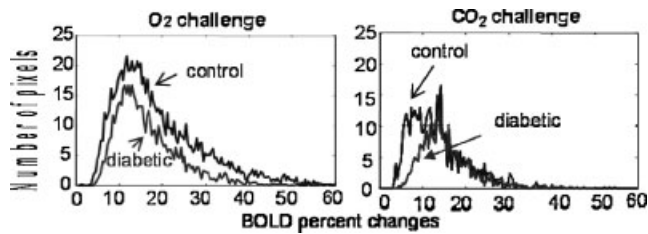


Figure 14. Anatomical and functional MRI of diabetic retinopathy. The numbers of activated pixels in all layers were diminished in diabetic animals 3 months after streptozotocin injection. Group-average histogram plots of number of pixels versus BOLD percentage changes. For O₂ challenge, the area under the curve for diabetes was 42% smaller than for controls ($P < 0.01$). For CO₂ challenge, the area under the curve for diabetes was 33% smaller than for controls ($P < 0.01$). This figure has appeared previously in abstract form (130).

the percentage change in activated pixels was not significantly different between diabetics and controls, the number of activated pixels in all layers was diminished in diabetic rats. Group-average histogram plots for the number of pixels versus BOLD percentage changes are shown in Fig. 14. For O₂ challenge, the area under the curve for diabetes was 42% smaller than for controls ($P < 0.01$, $n = 6$). For CO₂ challenge, the area under the curve for diabetes was 33% smaller than for controls ($P < 0.01$). Physiological fMRI thus has the potential to detect early onset of diabetic retinopathy and to stage the progression of early diabetic retinopathy.

The ΔPO_2 technique has also been used to study diabetic retinopathy. The carbogen-induced ΔPO_2 increase in rats with diabetic retinopathy was smaller than in control rats (44), suggesting a subnormal ΔPO_2 response in the early phase of diabetic retinopathy. In contrast, in human diabetic retinopathy, the ΔPO_2 increase was larger than in normal controls, and the ΔPO_2 increases were not dependent on diabetic retinopathy severity, the opposite of that of the rat data (40). The authors explained that this discrepancy was due to the differences in the length of hyperoxic exposure (131). Reduced Mn accumulation has also been reported in early diabetic retinopathy (42).

SUMMARY AND FUTURE PERSPECTIVES

This review summarizes the development and application of lamina-specific anatomical, physiological and functional MRI to the study of normal and diseased retinas. These MRI technologies reveal unique differential hemodynamic regulation in the two vascular layers of the retina. Some key advantages of MRI are its capacity to resolve depth information and provide comprehensive, layer-specific anatomical, physiological and functional information in a single setting. Key disadvantages of MRI include the lower spatial and temporal resolution

compared with optical imaging techniques. High-resolution MRI of the retina requires stability of the scanner and the eye. Optimization with FASTMAP shimming, custom eddy-current compensation for echo-planar imaging, image co-registration, and phase correction along the phase-encoding acquisition are important.

We predict that continuing advances in MRI technologies, including gradient performance, low-noise pre-amplifier, high-field scanners, novel pulse sequences, more sensitive detectors, and faster acquisition methods (such as parallel imaging to accelerate k-space acquisition), will broaden MRI applications in the retina. In return, the retina, with well-defined laminar structures, is an excellent model for advancing emerging high-resolution MRI technologies.

Although non-invasive MRI is expected to streamline human applications, much work remains before its clinical utility can be realized. The main challenges for layer-specific retinal MRI in awake humans are to minimize eye movement and to achieve sufficient spatial resolution given the clinical magnetic field gradient capability. With continuing advances in faster imaging techniques and improved gradient capability, we are hopeful that these challenges will be met. Nonetheless, MRI should readily serve as a valuable tool for studying normal retinal physiology and retinal diseases in animal models.

Acknowledgements

This research was supported by the NIH/NEI (R01 EY014211 to T.Q.D.), Whitaker Foundation (RG-02-0005, T.Q.D.), MERIT Awards (to M.T.P., P.M.T.) and Research Career Development Award (T.Q.D., D.E.O.) from the Department of Veterans Affairs, Emory University Research Committee (Q.S.), and the NIH/NEI (Ophthalmology Core grant, P30 EY006360). The Yerkes Imaging Center is supported in part by the NIH/NCRR base grant (P51 RR000165) and the Woodruff Health Science Center (T.Q.D). We value numerous insightful discussions with Dr Jeffrey W. Kiel, and Dr Robert A. Linsenmeier throughout this project.

REFERENCES

1. Kaufman PL, Alm A (eds). *Adler's Physiology of the Eye*. Mosby: St Louis, 1992.
2. Bron AJ, Tripathi RC, Tripathi BJ. *Wolff's Anatomy of the Eye and Orbit*. Chapman & Hall Medical: London, 1997.
3. Buttery RG, Hinrichsen CFL, Weller WL, J. R. H. How thick should a retina be? A comparative study of mammalian species with and without intraretinal vasculature. *Vision Res* 1991; **31**: 169–187.
4. Harris A, Kagemann L, Cioffi GA. Assessment of human ocular hemodynamics. *Surv Ophthalmol* 1998; **42**: 509–533.
5. Bill A. Circulation in the eye. In *Handbook of Physiology, Part 2, Microcirculation*, Renkin EM, Michel CC (eds). American Physiological Society: Bethesda, MD, 1984; 1001–1035.

6. Linsenmeier RA, Braun RD. Oxygen distribution and consumption in the cat retina during normoxia and hypoxemia. *J. Gen Physiol* 1992; **99**: 177–197.
7. Linsenmeier RA. Effects of light and darkness on oxygen distribution and consumption in the cat retina. *J. Gen Physiol* 1986; **88**: 521–542.
8. Yu D-I, Cringle SJ, Alder V, Su E-N. Intraretinal oxygen distribution in the rat with graded systemic hyperoxia and hypercapnia. *Invest Ophthalmol Vis Sci* 1999; **40**: 2082–2087.
9. Cheng H, Nair G, Walker TA, Kim MK, Pardue MT, Thule PM, Olson DE, Duong TQ. Structural and functional MRI reveals multiple retinal layers. *Proc Natl Acad Sci USA* 2006; **103**: 17525–17530.
10. Alm A, Bill A. Blood flow and oxygen extraction in the cat uvea at normal and high intraocular pressures. *Acta Physiol Scand* 1970; **80**: 19–28.
11. Friedman E, Kopald HH, Smith TR. Retinal and choroidal blood flow determined with krypton 85 in anesthetized animals. *Invest Ophthalmol* 1964; **3**: 539–547.
12. Linsenmeier RA, Padnick-Silver L. Metabolic dependence of photoreceptors on the choroid in the normal and detached retina. *Invest Ophthalmol Vis Sci* 2000; **41**: 3117–3123.
13. Parver LM. Choroidal blood flow as a heat dissipating mechanism in the macula. *Am J Ophthalmol* 1980; **89**: 641–646.
14. Parver LM, Auker CR, Carpenter DO, Doyle T. Choroidal blood flow. *Arch Ophthalmol* 1982; **100**: 1327–1330.
15. Fujimoto JG, Brezinski ME, Tearney GJ, Boppart SA, Bouma B, Hee MR, Southern JF, Swanson EA. Optical biopsy and imaging using optical coherence tomography. *Nat Med* 1995; **1**: 970–972.
16. Preussner PR, Richard G, Darrelmann O, Weber J, Kreissig I. Quantitative measurement of retinal blood flow in human beings by application of digital image-processing methods to television fluorescein angiograms. *Graefes Arch Clin Exp Ophthalmol* 1983; **221**: 110–112.
17. Guyer DR, Yannuzzi LA, Slakter JS, Sorenson JA, Orlock S. The status of indocyanine-green videoangiography. *Curr Opin Ophthalmol* 1993; **4**: 3–6.
18. Chauhan BC, Yu PK, Cringle SJ, Yu DY. Confocal scanning laser Doppler flowmetry in the rat retina: origin of flow signals and dependence on scan depth. *Arch Ophthalmol* 2006; **124**: 397–402.
19. Slakter JS, Yannuzzi LA, Guyer DR, Sorenson JA, Orlock DA. Indocyanine-green angiography. *Curr Opin Ophthalmol* 1995; **6**: 25–32.
20. Riva CE, Grunwald JE, Sinclair SH. Laser Doppler velocimetry study of the effect of pure oxygen breathing on retinal blood flow. *Invest Ophthalmol Vis Sci* 1983; **24**: 47–51.
21. Riva CE, Logean E, Falsini B. Visually evoked hemodynamical response and assessment of neurovascular coupling in the optic nerve and retina. *Prog Retinal Eye Res* 2005; **24**: 183–215.
22. Cheng H, Duong TQ. Simplified laser-speckle-imaging analysis method and its application to retinal blood flow imaging. *Opt Lett* 2007; **32**: 2188–2190.
23. Cheng H, Yan Y, Duong TQ. Temporal statistical analysis of laser speckle image and its application to retinal blood-flow imaging. *Optics Express* 2008; **16**: 10214–10219.
24. Silva AC, Koretsky AP. Laminar specificity of functional MRI onset times during somatosensory stimulation in rat. *Proc Natl Acad Sci USA* 2002; **99**: 15182–15187.
25. Goense JB, Logothetis NK. Laminar specificity in monkey V1 using high-resolution SE-fMRI. *Magn Reson Imag* 2006; **24**: 381–392.
26. Kim D-S, Duong TQ, Kim S-G. High-resolution mapping of iso-orientation columns by fMRI. *Nat Neurosci* 2000; **3**: 164–169.
27. Duong TQ, Kim D-S, Ugurbil K, Kim S-G. Localized blood flow response at sub-millimeter columnar resolution. *Proc Natl Acad Sci USA* 2001; **98**: 10904–10909.
28. Cheng K, Waggoner RA, Tanaka K. Human ocular dominance columns as revealed by high-field functional magnetic resonance imaging. *Neuron* 2001; **32**: 359–397.
29. Duong TQ, Kim D-S, Ugurbil K, Kim S-G. Spatio-temporal dynamics of the BOLD fMRI signals in cat visual cortex: toward mapping columnar structures using the early negative response. *Magn Reson Med* 2000; **44**: 231–242.
30. Shen Q, Cheng H, Pardue MT, Chang TF, Nair G, Vo VT, Shonat RD, Duong TQ. Magnetic resonance imaging of tissue and vascular layers in the cat retina. *J. Magn Reson Imaging* 2006; **23**: 465–472.
31. Chen J, Wang Q, Zhang H, Yang X, Wang J, Berkowitz BA, Wickline SA, Song SK. *In vivo* quantification of T(1), T(2), and apparent diffusion coefficient in the mouse retina at 11.74T. *Magn Reson Med* 2008; **59**: 731–738.
32. Nair G, Cheng H, Duong TQ. Layer-specific manganese-enhanced MRI of retinal degeneration in RCS rats. *Society for Neuroscience* 2006; Atlanta, GA: p. 489.
33. Nair G, Cheng H, Kim M, Walker TA, Olson DE, Thulé PM, Pardue MT, Duong TQ. Manganese-enhanced MRI reveals multiple cellular and vascular layers in normal and degenerated retinas. *Proc Int Soc Magn Reson Med*. 2007; Berlin, Germany: p. 2452.
34. Li Y, Cheng H, Duong TQ. Blood-flow magnetic resonance imaging of the retina. *Neuroimage* 2008; **39**: 1744–1751.
35. Duong TQ, Ngan SC, Ugurbil K, Kim SG. Functional magnetic resonance imaging of the retina. *Invest Ophthalmol Vis Sci* 2002; **43**: 1176–1181.
36. Berkowitz BA, Wilson CA. Quantitative mapping of ocular oxygenation using magnetic resonance imaging. *Magn Reson Med* 1995; **33**: 579–581.
37. Luan H, Roberts R, Sniegowski M, Goebel DJ, Berkowitz BA. Retinal thickness and subnormal retinal oxygenation response in experimental diabetic retinopathy. *Invest Ophthalmol Vis Sci* 2006; **47**: 320–328.
38. Wilson DF, Pastuszko A, DiGiacomo JE, Pawlowski M, Schneiderman R, Delivoria-Papadopoulos M. Effect of hyperventilation on oxygenation of the brain cortex of newborn piglets. *J. Appl Physiol* 1991; **70**: 2691–2696.
39. Berkowitz BA. Adult and newborn rat inner retinal oxygenation during carbogen and 100% oxygen breathing. Comparison using magnetic resonance imaging delta PO₂ mapping. *Invest Ophthalmol Vis Sci* 1996; **37**: 2089–2098.
40. Trick GL, Edwards P, Desai U, Berkowitz BA. Early supernormal retinal oxygenation response in patients with diabetes. *Invest Ophthalmol Vis Sci* 2006; **47**: 1612–1619.
41. Berkowitz BA, Roberts R, Goebel DJ, Luan H. Noninvasive and simultaneous imaging of layer-specific retinal functional adaptation by manganese-enhanced MRI. *Invest Ophthalmol Vis Sci* 2006; **47**: 2668–2674.
42. Berkowitz BA, Roberts R, Stemmler A, Luan H, Gradianu M. Impaired apparent ion demand in experimental diabetic retinopathy: correction by lipoic Acid. *Invest Ophthalmol Vis Sci* 2007; **48**: 4753–4758.
43. Berkowitz BA, Roberts R, Penn JS, Gradianu M. High-resolution manganese-enhanced MRI of experimental retinopathy of prematurity. *Invest Ophthalmol Vis Sci* 2007; **48**: 4733–4740.
44. Berkowitz BA, Kowluru RA, Frank RN, Kern TS, Hohman TC, Prakash M. Subnormal retinal oxygenation response precedes diabetic-like retinopathy. *Invest Ophthalmol Vis Sci* 1999; **40**: 2100–2105.
45. Vinore SA. Assessment of blood-retinal barrier integrity. *Histol Histopathol* 1995; **10**: 141–154.
46. Duong TQ, Shen Q, Cheng H, Chang TF, Shonat RD. Magnetic resonance imaging of anatomical layers in the cat retina. In: *Invest Ophthalmol Vis Sci* 2005; Suppl: 1049.
47. Shen Q, Cheng H, Chang T, Nair G, Shonat RD, Duong TQ. Magnetic resonance imaging of anatomical layers of the cat retina. *Proc Int Soc Magn Reson Med*, 2005; Miami, FL: p. 1033.
48. Eaton AM, Hatchell DL. Measurement of retinal blood vessel width using computerized image analysis. *Invest Ophthalmol Vis Sci* 1988; **29**: 1258–1264.
49. Newsom RS, Sullivan PM, Rassam SM, Jagoe R, Kohner EM. Retinal vessel measurement: comparison between observer and computer driven methods. *Graefes Arch Clin Exp Ophthalmol* 1992; **30**: 221–225.
50. Roy CS, Sherrington CS. On the regulation of blood supply of the brain. *J. Physiol* 1890. **1**: 85–108.
51. Riva CE, Harino S, Shonat RD, Petrig BL. Flicker evoked increase in optic nerve head blood flow in anesthetized cats. *Neurosci Lett* 1991; **128**: 291–296.

52. Mandecka A, Dawczynski J, Blum M, Muller N, Kloos C, Wolf G, Vilser W, Hoyer H, Muller UA. Influence of flickering light on the retinal vessels in diabetic patients. *Diabetes Care* 2007; **30**: 3048–3052.
53. Yu D-Y, Cringle SJ, Su E-N, Yu PK. Intraretinal oxygen levels before and after photoreceptor loss in the RCS rat. *Invest Ophthalmol Vis Sci* 2000; **41**: 3999–4006.
54. Grinvald A, Bonhoeffer T, Vanzetta I, Pollack A, Aloni E, Ofri R, Nelson D. High-resolution functional optical imaging: from the neocortex to the eye. *Ophthalmol Clin North Am* 2004; **17**: 53–67.
55. Zarella MD, Li H, Kwon Y, Kardon R, Soliz P, Tso DY. The origins and spatio-temporal properties of stimulus dependent intrinsic optical signals of the retina. *Society for Neuroscience*, 2004; Program No. 934.910.
56. Ogawa S, Lee T-M, Kay AR, Tank DW. Brain magnetic resonance imaging with contrast dependent on blood oxygenation. *Proc Natl Acad Sci USA* 1990; **87**: 9868–9872.
57. Ogawa S, Tank DW, Menon R, Ellermann JM, Kim S-G, Merkle H, Ugurbil K. Intrinsic signal changes accompanying sensory stimulation: functional brain mapping with magnetic resonance imaging. *Proc Natl Acad Sci USA* 1992; **89**: 5951–5955.
58. Kwong K, Hoppel B, Weisskoff R, Kiihne S, Barrere B, Moore J, Poncelet B, Rosen B, Thulborn K. Regional cerebral tissue oxygenation studied with EPI at clinical field strengths. *J. Magn Reson Imag* 1992; **2**: 44.
59. Bandettini PA, Wong EC, Hinks RS, Rikofsky RS, Hyde JS. Time course EPI of human brain function during task activation. *Magn Reson Med* 1992; **25**: 390–397.
60. Logothetis NK, Pauls J, Augath M, Trinath T, Oeltermann A. Neurophysiological investigation of the basis of the fMRI signal. *Nature* 2001; **412**: 150–157.
61. Duong TQ, Kim DS, Ugurbil K, Kim SG. Localized cerebral blood flow response at submillimeter columnar resolution. *Proc Natl Acad Sci USA* 2001; **98**: 10904–10909.
62. Posse S, Elghahwagi B, Wiess S, Kiselev VG. Effect of graded hypo- and hypercapnia on fMRI contrast in visual cortex: quantification of T_2^* changes by multiecho EPI. *Magn Reson Med* 2001; **46**: 264–271.
63. Cohen ER, Ugurbil K, Kim S-G. Effect of basal conditions on the magnitude and dynamics of the blood oxygenation level-dependent fMRI response. *J. Cereb Blood Flow Metab* 2002; **22**: 1042–1053.
64. Sicard KM, Duong TQ. Effects of hypoxia, hyperoxia and hypercapnia on baseline and stimulus-evoked BOLD, CBF and $CMRO_2$ in spontaneously breathing animals. *Neuroimage* 2005; **25**: 850–858.
65. Duong TQ, Iadacola C, Kim S-G. Effect of hyperoxia, hypercapnia and hypoxia on cerebral interstitial oxygen tension and cerebral blood flow in the rat brain: an $^{19}F/^1H$ study. *Magn Reson Med* 2001; **45**: 61–70.
66. Trokel S. Effect of respiratory gases upon choroidal hemodynamics. *Arch Ophthalmol* 1965; **73**: 838–842.
67. Kety SS, Schmidt CF. The effects of altered arterial tensions of carbon dioxide and oxygen on cerebral blood flow and cerebral oxygen consumption of normal young men. *J. Clin Invest* 1948; **27**: 484–491.
68. Riva CE, Cranstoun SD, Mann RM, Barnes GE. Local choroidal blood flow in the cat by laser Doppler flowmetry. *Invest Ophthalmol Vis Sci* 1994; **35**: 608–618.
69. Ogawa S, Menon RS, Tank DW, Kim SG, Merkle H, Ellermann JM, Ugurbil K. Functional brain mapping by blood oxygenation level-dependent contrast magnetic resonance imaging. A comparison of signal characteristics with a biophysical model. *Biophys J* 1993; **64**: 803–812.
70. Calamante F, Gadian DG, Connelly A. Quantification of perfusion using bolus tracking magnetic resonance imaging in stroke: assumptions, limitations, and potential implications for clinical use. *Stroke* 2002; **33**: 1146–1151.
71. Alsop D, Detre J. Reduced transit-time sensitivity in noninvasive magnetic resonance imaging of human cerebral blood flow. *J. Cereb Blood Flow Metab* 1996; **16**: 1236–1249.
72. Wong EC, Buxton RB, Frank LR. Quantitative imaging of perfusion using a single subtraction (QUIPSS and QUIPSSII). *Magn Reson Med* 1998; **39**: 702–708.
73. Wong EC, Buxton RB, Frank LR. A theoretical and experimental comparison of continuous and pulsed arterial spin labeling techniques for quantitative perfusion imaging. *Magn Reson Med* 1998; **40**: 348–355.
74. Detre JA, Zhang W, Roberts DA, Silva AC, Williams DS, Grandis DJ, Koretsky AP, Leigh JS. Tissue specific perfusion imaging using arterial spin labeling. *NMR Biomed* 1994; **7**: 75–82.
75. Williams DS, Detre JA, Leigh JS, Koretsky AP. Magnetic resonance imaging of perfusion using spin inversion of arterial water. *Proc Natl Acad Sci USA* 1992; **89**: 212–216.
76. Duong TQ, Silva AC, Lee S-P, Kim S-G. Functional MRI of calcium-dependent synaptic activity: cross correlation with CBF and BOLD measurements. *Magn Reson Med* 2000; **43**: 383–392.
77. Tsekos NV, Zhang F, Merkle H, Nagayama M, Iadecola C, Kim S-G. Quantitative measurements of cerebral blood flow in rats using the FAIR technique: correlation with previous iodoantipyrine autoradiographic studies. *Magn Reson Med* 1998; **39**: 564–573.
78. Zaini MR, Strother SC, Andersen JR, Liow J-S, Kjems U, Tegeler C, Kim S-G. Matching spatial resolution of coregistered PET and 4.0T fMRI brain volumes. *Med Phys* 1999; **26**: 1559–1567.
79. Liu HL, Kochunov P, Hou J, Pu Y, Mahankali S, Feng CM, Yee SH, Wan YL, Fox PT, Gao JH. Perfusion-weighted imaging of interictal hypoperfusion in temporal lobe epilepsy using FAIR-HASTE: comparison with $H(2)(15)O$ PET measurements. *Magn Reson Med* 2001; **45**: 431–435.
80. Meng X, Fisher M, Shen Q, Sotak CH, Duong TQ. Characterizing the diffusion/perfusion mismatch in experimental focal cerebral ischemia. *Ann Neurol* 2004; **55**: 207–212.
81. Shen Q, Meng X, Fisher M, Sotak CH, Duong TQ. Pixel-by-pixel spatiotemporal progression of focal ischemia derived using quantitative perfusion and diffusion imaging. *J. Cereb Blood Flow Metab* 2003; **23**: 1479–1488.
82. Shen Q, Fisher M, Sotak CH, Duong TQ. Effects of reperfusion on ADC and CBF pixel-by-pixel dynamics in stroke: characterizing tissue fates using quantitative diffusion and perfusion imaging. *J. Cereb Blood Flow Metab* 2004; **24**: 280–290.
83. Shen Q, Ren H, Cheng H, Fisher M, Duong TQ. Functional, perfusion and diffusion MRI of acute focal ischemic brain injury. *J. Cereb Blood Flow Metab* 2005; **25**: 1265–1279.
84. Herscovitch P, Raichle ME. What is the correct value for the brain-blood partition coefficient for water? *J Cereb Blood Flow Metab* 1985; **5**: 65–69.
85. Liu ZM, Schmidt KF, Sicard KM, Duong TQ. Imaging oxygen consumption in forepaw somatosensory stimulation in rats under isoflurane anesthesia. *Magn Reson Med* 2004; **52**: 277–285.
86. Alm A, Bill A. Ocular and optic nerve blood flow at normal and increased intraocular pressures in monkeys (*Macaca irus*): a study with radioactively labeled microspheres including flow determinations in brain and some other tissues. *Exp Eye Res* 1973; **15**: 15–29.
87. Wang L, Fortune B, Cull G, McElwain KM, Cioffi GA. Microspheres method for ocular blood flow measurement in rats: size and dose optimization. *Exp Eye Res* 2007; **84**: 108–117.
88. Matta BF, Heath KJ, Tipping K, Summers AC. Direct cerebral vasodilatory effects of sevoflurane and isoflurane. *Anesthesiology* 1999; **91**: 677–680.
89. Sicard K, Shen Q, Brevard M, Sullivan R, Ferris CF, King JA, Duong TQ. Regional cerebral blood flow and BOLD response in conscious and anesthetized rats under basal and hypercapnic conditions: implications for fMRI studies. *J. Cereb Blood Flow Metab* 2003; **23**: 472–481.
90. Duong TQ, Kim S-G. *In vivo* MR measurements of regional arterial and venous blood volume fractions in intact rat brain. *Magn Reson Med* 2000; **43**: 392–402.
91. Duong TQ, Ngan S-C, Ugurbil K, Kim S-G. Functional magnetic resonance imaging of the retina. *Invest Ophthalmol Vis Sci* 2002; **43**: 1176–1181.
92. Cotzias G, Horiuchi M, Fuenzalida S, Mena I. Clearance of tissue manganese concentrations with persistence of the neurological picture. *Neurology* 1968; **18**: 376–382.
93. Newland M, Cox C, Hamada R, Oberdoerster G, Weiss R. The clearance of manganese chloride in the primate. *Fundam Appl Toxicol* 1987; **9**: 314–328.

94. Lin Y-J, Koretsky AP. Manganese ion enhances T1-weighted MRI during brain activation: an approach to direct imaging of brain function. *Magn Reson Med* 1997; **38**: 378–398.
95. Pautler RG, Koretsky AP. Tracing odor-induced activation in the olfactory bulbs of mice using manganese-enhanced magnetic resonance imaging. *Neuroimage* 2002; **16**: 441–448.
96. Silva AC, Lee JH, Aoki I, Koretsky AP. Manganese-enhanced magnetic resonance imaging (MEMRI): methodological and practical considerations. *NMR Biomed* 2004; **17**: 532–543.
97. Pautler RG. Biological applications of manganese-enhanced magnetic resonance imaging. *Methods Mol Med* 2006; **124**: 365–386.
98. Lee JH, Silva AC, Merkle H, Koretsky AP. Manganese-enhanced magnetic resonance imaging of mouse brain after systemic administration of MnCl₂: dose-dependent and temporal evolution of T1 contrast. *Magn Reson Med* 2005; **53**: 640–648.
99. Aoki I, Wu YJ, Silva AC, Lynch RM, Koretsky AP. *In vivo* detection of neuroarchitecture in the rodent brain using manganese-enhanced MRI. *Neuroimage* 2004; **22**: 1046–1059.
100. Chan KC, Fu QL, Hui ES, So KF, Wu EX. Evaluation of the retina and optic nerve in a rat model of chronic glaucoma using *in vivo* manganese-enhanced magnetic resonance imaging. *Neuroimage* 2008; **40**: 1166–1174.
101. Berson EL. Retinitis pigmentosa: unfolding its mystery. *Proc Natl Acad Sci USA* 1996; **93**: 4526–4528.
102. Sieving PA, Caruso RC, Tao W, Coleman HR, Thompson DJ, Fullmer KR, Bush RA. Ciliary neurotrophic factor (CNTF) for human retinal degeneration: phase I trial of CNTF delivered by encapsulated cell intraocular implants. *Proc Natl Acad Sci USA* 2006; **103**: 3896–3901.
103. Chao HM, Chidlow G, Melena J, Wood JP, Osborne NN. An investigation into the potential mechanisms underlying the neuroprotective effect of clonidine in the retina. *Brain Res* 2000; **877**: 47–57.
104. Acland GM, Aguirre GD, Ray J, Zhang Q, Aleman TS, Cideciyan AV, Pearce-Kelling SE, Anand V, Zeng Y, Magure AM, Jacobson SG, Hauswirth WW, Bennett J. Gene therapy restores vision in a canine model of childhood blindness. *Nat Genet* 2001; **28**: 92–95.
105. Rizzo JFr, Wyatt J, Humayun M, de Juan E, Liu W, Chow A, Eckmiller R, Zrenner E, Yagi T, Abrams G. Retinal prosthesis: an encouraging first decade with major challenges ahead. *Ophthalmology* 2001; **108**: 13–14.
106. Gal A, Li Y, Thompson DA, Weir J, Orth U, Jacobson SG, Apfelstedt-Sylla E, Vollrath D. Mutations in MERTK, the human orthologue of the RCS rat retinal dystrophy gene, cause retinitis pigmentosa. *Nat Genet* 2000; **26**: 270–271.
107. D'Cruz PM, Yasumura D, Weir J, Matthes MT, Abderrahim H, LaVail MM, Vollrath D. Mutation of the receptor tyrosine kinase gene Mertk in the retinal dystrophic RCS rat. *Hum Mol Genet* 2000; **9**: 645–651.
108. Mullen RJ, LaVail MM. Inherited retinal dystrophy: primary defect in pigment epithelium determined with experimental rat chimeras. *Science* 1976; **192**: 799–801.
109. Dowling JE, Sidman RL. Inherited retinal dystrophy in the rat. *J. Cell Biol* 1962; **14**: 73–109.
110. Ball S, Hanzlicek B, Blum M, Pardue MT. Evaluation of inner retinal structure in the aged RCS rat. *Adv Exp Med Biol* 2003; **533**: 181–188.
111. Milam AH, Li ZY, Fariss RN. Histopathology of the human retina in retinitis pigmentosa. *Prog Retinal Eye Res* 1998; **17**: 175–205.
112. Padnick-Silver L, Kang Derwent JJ, Giuliano E, Narfstrom K, Linsenmeier RA. Retinal oxygenation and oxygen metabolism in Abyssinian cats with a hereditary retinal degeneration. *Invest Ophthalmol Vis Sci* 2006; **47**: 3683–3689.
113. Li Y, Cheng H, Shen Q, Kim M, Olson DE, Thule PM, Pardue MT, Duong TQ. Blood-flow MRI of retinal degeneration. *Proc Int Soc Magn Reson Med*, 2008; Toronto, Canada: p. 1872.
114. Aiello LP, Gardner TW, King GL, Blankenship G, Cavallerano JD, Ferris FL, Klein R. Diabetic retinopathy. *Diabetes Care* 1998; **21**: 143–156.
115. Alder VA, Su EN, Yu DY, Cringle SJ, Yu PK. Diabetic retinopathy: early functional changes. *Clin Exp Pharm Physiol* 1997; **24**: 785–788.
116. No-author. Early worsening of diabetic retinopathy in the Diabetes Control and Complications Trial. *Arch Ophthalmol* 1998; **116**: 874–886.
117. Frank RN. On the pathogenesis of diabetic retinopathy: a 1990 update. *Ophthalmology* 1991; **98**: 586–593.
118. Patz A. Studies on retinal neovascularization: Friedenwald Lecture. *Invest Ophthalmol Vis Sci* 1980; **19**: 1133–1138.
119. Stefansson E. Ocular oxygenation and the treatment of diabetic retinopathy. *Surv Ophthalmol* 2006; **51**: 364–380.
120. Stefansson E. Oxygen and diabetic eye disease. *Graefes Arch Ophthalmol* 1990; **228**: 120–123.
121. Stefansson E, Hatchell DL, Fisher BL, Sutherland FS, Machermer R. Panretinal photocoagulation and retinal oxygenation in normal and diabetic cats. *Am J Ophthalmol* 1986; **101**: 657–664.
122. Molnar I, Poitry IS, Tsacopoulos M, Gilodi N, Leuenberger PM. Effect of laser photocoagulation on oxygenation of the retina in miniature pigs. *Invest Ophthalmol Vis Sci* 1985; **26**: 1410–1414.
123. Landers MB III, Stefansson E, Wolbarsht ML. Panretinal photocoagulation and retinal oxygenation. *Retina* 1982; **2**: 167–175.
124. Grunwald JE, Riva CE, Brucker AJ, Sinclair SH, Petrig BL. Effect of panretinal photocoagulation on retinal blood flow in proliferative diabetic retinopathy. *Ophthalmology* 1986; **93**: 590–595.
125. Alder VA, Cringle SJ, Brown M. The effect of regional retinal photocoagulation on vitreal oxygen tension. *Invest Ophthalmol Vis Sci* 1987; **28**: 1078–1085.
126. Shimada Y, Li Y, Bearse M, Sutter E, Fung W. Assessment of early retinal changes in diabetes using a new multifocal ERG protocol. *Br J Ophthalmol* 2001; **85**: 414–419.
127. Grunwald JE, Riva E, Brucker CEAJ, Sinclair SH, Petrig BL. Altered retinal vascular response to 100% oxygen breathing in diabetes mellitus. *Ophthalmology* 1984; **91**: 1447–1452.
128. Grunwald JE, Riva CE, Baine J, Brucker AJ. Total retinal volumetric blood flow rate in diabetic patients with poor glycemic control. *Invest Ophthalmol Vis Sci* 1992; **33**: 356–363.
129. Linsenmeier RA. The role of the choroidal circulation in the retinal oxygenation. *XIIIe Int Congress Eye Res Paris*, 1998; Paris: p. S13.
130. Cheng H, Olson DE, Liu Y, Thule PM, Pardue MT, Duong TQ. Lamina-specific anatomical and functional imaging of normal and diabetic retina. *Proc Int Soc Magn Reson Med*, 2006; Seattle, Washington: p. 806.
131. Roberts R, Luan H, Berkowitz BA. Alpha-lipoic acid corrects late-phase supernormal retinal oxygenation response in experimental diabetic retinopathy. *Invest Ophthalmol Vis Sci* 2006; **47**: 4077–4082.
132. Shen Q, Ren H, Bouley J, Fisher M, Duong TQ. Dynamic tracking of acute ischemic tissue fates using improved unsupervised ISODATA analysis of high-resolution quantitative perfusion and diffusion data. *J. Cereb Blood Flow Metab* 2004; **24**: 887–897.